

# Assessment of Passive Flow Control for Transonic Cavity Flow Using Detached-Eddy Simulation

S. J. Lawson\* and G. N. Barakos†

University of Liverpool, Liverpool, England L63 3GH, United Kingdom

DOI: 10.2514/1.39894

The implementation of internal store carriage on stealthy military aircraft has accelerated research into transonic cavity flows. Depending on the freestream Mach number and the cavity dimensions, flows inside cavities can become unsteady, threatening the structural integrity of the cavity and its contents (e.g., stores, avionics, etc.). Below a critical length-to-depth ratio, the shear layer formed along the cavity mouth has enough energy to span across the opening. This shear layer impacts the downstream cavity corner and the generated acoustic disturbances propagate upstream, causing further instabilities near the cavity front. Consequently, a self-sustained feedback loop is established. This extreme flow environment calls for flow control ideas aiming to pacify the cavity by breaking the feedback loop and controlling the breakdown of the shear layer. This is the objective of the present work, which aims to assess changes of the cavity geometry and their effect on the resulting flow using detached-eddy simulation. For the cases computed in this work, quantitative and qualitative agreement with experimental data has been obtained. All of the devices tested achieved similar reductions in overall sound pressure level in the rear half of the cavity; however, a slanted aft wall provided the largest noise reduction in the front half of the cavity.

## Nomenclature

$A$	= wall area, m <sup>2</sup>
$a_i(t)$	= temporal eigenfunctions
$C_F$	= force coefficient
$D$	= cavity depth, m
$F, G, H$	= spatial flux vectors in Navier–Stokes equations
$f$	= frequency, Hz
$L$	= cavity length, m
$N$	= number of snapshots for proper orthogonal decomposition
$p$	= pressure, Pa
$p'$	= unsteady pressure, Pa
$Q$	= unsteady terms in Navier–Stokes equations
$q_\infty$	= freestream dynamic pressure ( $\frac{1}{2}\rho_\infty U_\infty^2$ ), Pa
$Re$	= Reynolds number
$Re_L$	= Reynolds number based on cavity length $L$
$\mathbf{S}$	= symmetric components of the velocity gradient tensor [Eq. (7)]
$\mathbf{S}$	= source vector in Navier–Stokes equations [Eq. (1)]
$T_{\text{Rossiter1}}$	= time period of the lowest Rossiter mode, s
$t$	= time, s
$u$	= velocity, m/s
$x, y, z$	= Cartesian coordinates, m
$\lambda_i$	= matrix eigenvalues
$\rho$	= density, kg/m <sup>3</sup>
$\Phi_i(x)$	= spatial eigenfunctions
$\mathbf{\Omega}$	= antisymmetric component of the velocity gradient tensor

## Subscripts

rms	= root mean square
$m$	= mean quantity
$\infty$	= freestream value

## Superscripts

inv	= inviscid term
vis	= viscous term

## I. Introduction

THE next generation of military aircraft, such as uninhabited combat air vehicles, has been designed to avoid detection. To minimize the radar cross section, loads normally carried on pylons under the wings are now being stored internally. This recent interest in internal carriage of stores has accelerated research in flows surrounding weapons bays; however, the mechanisms that drive cavity flows need to be better understood.

Depending on the freestream Mach number and the cavity dimensions, the flow inside the cavity can become very unsteady. For a length-to-depth  $L/D$  ratio of less than 10, the shear layer has enough energy to span across the cavity opening. When the shear layer impacts the downstream cavity corner, pressure disturbances are generated and propagated upstream, which in turn causes further instabilities at the cavity front, and a feedback loop is established [1]. The acoustic environment in the cavity is so harsh in these circumstances that the noise level at the cavity rear has been found to approach 170 dB, and frequencies near 1 kHz are created [2]. The effect of this unsteady environment on the structural integrity of the contents of the cavity (e.g., stores, avionics, etc.) can be serious. Above an  $L/D$  ratio of 14, the shear layer no longer has enough energy to span across the cavity and dips into it. Although this does not produce noise levels and frequencies as high as in shorter cavities, the pressure differential along the cavity produces large pitching moments, making store release difficult.

Cavity flow research is not limited to military applications. Examples of other areas include the noise suppression of the undercarriage wheel wells on airliners or even car-cabin noise in the presence of open sunroofs. Flows surrounding wheel wells are considered to be one of the primary sources of noise during the landing

This paper is dedicated to the memory of John Ross, who contributed the experiments for this cavity flow study.

Received 20 July 2008; revision received 11 November 2008; accepted for publication 16 November 2008. Copyright © 2008 by the authors. Published by the American Institute of Aeronautics and Astronautics, Inc., with permission. Copies of this paper may be made for personal or internal use, on condition that the copier pay the \$10.00 per-copy fee to the Copyright Clearance Center, Inc., 222 Rosewood Drive, Danvers, MA 01923; include the code 0021-8669/09 \$10.00 in correspondence with the CCC.

\*Ph.D. Candidate, Computational Fluid Dynamics Laboratory, Department of Engineering; S.J.Lawson@liverpool.ac.uk.

†Reader, Computational Fluid Dynamics Laboratory, Department of Engineering; G.Barakos@Liverpool.ac.uk (Corresponding Author).

approach and touchdown. Methods to alleviate this problem are being considered by several researchers. Reference [3] is a good example of these efforts.

Ever since the problems associated with cavity flows were realized, much research into methods to improve the cavity environment has been undertaken. Some control methods involved manipulating the cavity geometry by either modifying the angle at which the cavity walls are slanted or by adding external devices to deliberately alter the flow inside the cavity. Such techniques are referred to here as *passive* flow control devices. The second type, known as *active* flow control, involves altering the flow within the cavity through the addition of devices that require external energy input. This includes devices such as jets or oscillating flaps. Active flow control can be either of the open- or closed-loop type. Closed-loop control requires the implementation of a feedback loop in the control method, which allows the method to continually adapt to the flight conditions, thus making them more suitable for time-varying and offdesign situations. Although open-loop control studies have dominated most control efforts in cavity flows, examples of closed-loop cavity control studies are also beginning to appear in literature. For more information on the cavity-flow control, the reader is directed to the excellent review by Cattafesta et al. [4], which provides an account of

different open-loop and closed-loop control strategies adopted by various researchers.

### A. Experimental Studies

Flows over cavities have been studied experimentally since the implementation of weapons bays into military aircraft in the mid-1950s [5–7]. In high Reynolds number flows, a broad range of turbulent length and time scales exist. For cavity flow, this intense turbulent environment is further coupled with strong acoustic radiation, the source of which is located at the downstream corner of the cavity. The acoustical signature in the cavity is composed of two parts: broadband noise and narrowband tones. The broadband is low-energy noise contributed by the freestream, the shear layer, and turbulent fluctuations. The tones, called Rossiter modes [7] (named after J. E. Rossiter, who developed a semi-empirical formula to calculate the frequencies at which they occur), can vary in magnitude and are caused by specific interactions in the flow. These could include vortex–vortex, vortex/wall, vortex/shear-layer, shock/shear-layer, and shear-layer/wall interactions.

Most cavity experiments were based on unsteady pressure measurements in wind tunnels. The works of Tracy et al. [8] and Tracy and Plentovich [9,10] from NASA Langley and Ross and

**Table 1 Summary of selected clean-cavity experimental studies**

Clean cavity					
Study	Geometry		Flow conditions		Instrumentation
	$L/D$	$W/D$	Mach no.	$Re_L$	
Shaw et al. [16]	6.79,10.27	—	0.7–2.0	—	Dynamic pressure transducers
Tracy et al. [8]	4.4–20	0.97–4.4	0.2–0.9	$1.8–93.8 \times 10^6$	Dynamic pressure transducers
Plentovich et al. [17]	1–17.5	1–16	0.2–0.95	$0.3–10.5 \times 10^6$	Static pressure taps
Tracy and Plentovich [9]	4.4–20	0.97–4.4	0.2–0.9	$28.1 \times 10^6$	Static and dynamic pressure transducers
Stallings et al. [18]	6.7–17.5	2.4	0.2–0.95	$5.4–12.6 \times 10^6$	Static pressure taps
Stallings et al. [19]	5.42–12.50	2.4	0.2–0.95	$4.3–11.8 \times 10^6$	Static pressure taps
Tracy and Plentovich [10]	1–17.5	1–16	0.2–0.95	$0.3–10.5 \times 10^6$	Dynamic pressure transducers
Chung [20,21]	2.43–43	1.2–86	1.28	$4.5 \times 10^6$	Dynamic pressure transducers
Chung [22]	2.43–43	2.43–43	0.33–0.82	$1.8–3.6 \times 10^6$	Dynamic pressure transducers
Ritchie et al. [15]	5	2.5	0.82	—	Particle image velocimetry (PIV)
Kegerise et al. [23]	2.4	1	0.2–0.6	$1.5 \times 10^6$	Dynamic pressure transducers and schlieren
Nightingale et al. [14]	5	1	0.6–1.35	$6.5 \times 10^6$	Dynamic pressure transducers, PIV

**Table 2 Summary of selected experimental studies of passive flow control**

Experimental						
Study	Geometry		Flow Conditions		Instrumentation	Flow Control <sup>a</sup>
	$L/D$	$W/D$	Mach No.	$Re_L$		
Shaw et al. [16]	6.79,10.27	—	0.7–2.0	—	Dynamic pressure transducers	SW, STS, TR
Sarno and Franke [24]	2	0.3	0.6–1.5	$1–3.6 \times 10^6$	Dynamic pressure transducers	FTS
Stallings et al. [18]	6.7–17.5	2.4	0.2–0.95	$5.4–12.6 \times 10^6$	Static pressure taps	Slotted/vented wall/floor
Ross and Peto [12]	5,10	1,2	0.85–1.35	$6.5 \times 10^6$	Dynamic pressure transducers	SW, STS
Smith et al. [25]	4.6–7.27	1.85–2.91	0.9,1.5	—	Dynamic pressure transducers	TR
Ukeiley et al. [26]	5.6,9.0	2	0.6, 0.75	$0.1–0.3 \times 10^6$	Dynamic pressure transducers	TR, FTS
Nightingale et al. [14]	5	1	0.85	$6.5 \times 10^6$	Dynamic pressure transducers, PIV	SW, STS, FTS, TR

<sup>a</sup>SW denotes slanted walls, STS denotes the sawtooth spoiler, FTS denotes the flattop spoiler, and TR denotes the transverse rod.

**Table 3 Summary of selected numerical studies of passive flow control**

CFD						
Study	Geometry		Flow conditions		Method	Flow control
	$L/D$	$W/D$	Mach no.	$Re_L$		
Baysal et al. [27]	4.5	—	0.95	$8 \times 10^6/m$	2-D RANS, B-L model	SW, FTS
Arunajatesan et al. [28]	5.6	1	0.6	$1.45 \times 10^7/m$	Hybrid $k-\epsilon$ RANS-LES	TR
Nayyar [2]	5	1	0.85	$1 \times 10^6$	2-D URANS	SW, FTS
Comte et al. [29]	0.42	1	0.85	$0.86 \times 10^6$	LES, DES	TR
Ashworth [30]	5	1	0.85	—	DES	STS

**Table 4 Summary of selected numerical studies of clean-cavity flows**

Study	Clean cavity				Method
	Geometry		Flow conditions		
	$L/D$	$W/D$	Mach no.	$Re_L$	
Rizzetta [34]	5.07	2.67	1.5	$1.09 \times 10^6$	2-D and 3-D RANS (Baldwin–Lomax turbulence model)
Srinivasan and Baysal [32]	4.4, 11.7	1.2, 7	0.9, 0.58	$5.6, 5.32 \times 10^6$	3-D RANS (Baldwin–Lomax turbulence model)
Sinha et al. [45]	6, 4.5	—	1.5, 2	$4.5 \times 10^6$	Hybrid RANS/LES
Arunajatesan et al. [28]	5.6	1	0.6	$1.45 \times 10^7/m$	Hybrid RANS/LES
Gloerfelt et al. [46]	3	3.85	0.8	$0.14 \times 10^6$	LES
Hamed et al. [42, 43]	5	0.5	1.19	$0.2, 1 \times 10^6$	DES
Mendonça et al. [44]	5	1	0.85	—	URANS and DES
Rizzetta and Visbal [37]	5	0.5	1.19	$0.2 \times 10^6$	LES
Ritchie et al. [15]	5	2.5	0.82	—	2-D RANS ( $k-\varepsilon$ turbulence model)
Larchevêque et al. [38]	0.42	1	0.8	$0.86 \times 10^6$	Monotone integrated LES (MILES)
Larchevêque et al. [39]	5	1	0.85	$7 \times 10^6$	MILES
Nayyar [2]	2, 16	1	0.85	$1, 6.8 \times 10^6$	URANS, LE, and DES
Nayyar et al. [41]	5	1	0.85	$1 \times 10^6$	URANS, LES, and DES
Lai and Luo [47]	5	1	0.85	$1.36 \times 10^6$	LES
Larchevêque et al. [40]	2	4.8	0.85	$0.86 \times 10^6$	MILES
Peng and Leicher [48]	5	1	0.85	—	DES and hybrid RANS-LES

**Table 5 Kulite positions in QinetiQ experiments for  $L/D = 5$  cavity [14]**

Location	Tag	Kulite position		
		$x/L$	$y/L$	$z/L$
Front plate	K1	-0.35	0.0	0.0
	K2	-0.20	0.0	0.0
Aft plate	K4	1.95	0.0	-0.1375
	K7	0.0	-0.05	0.1250
Front wall	K8	0.0	-0.05	-0.0250
	K20	0.05	-0.20	0.0
Floor	K21	0.15	-0.20	0.0
	K22	0.25	-0.20	0.0
	K23	0.35	-0.20	0.0
	K24	0.45	-0.20	0.0
	K25	0.55	-0.20	0.0
	K26	0.65	-0.20	0.0
	K27	0.75	-0.20	0.0
	K28	0.85	-0.20	0.0
	K29	0.95	-0.20	0.0
	Rear wall	K17	1.0	-0.0375
K18		1.0	-0.0750	0.1375
K82		1.0	-0.0750	0.0
K83		1.0	-0.1250	0.0
K84		1.0	-0.1750	0.0

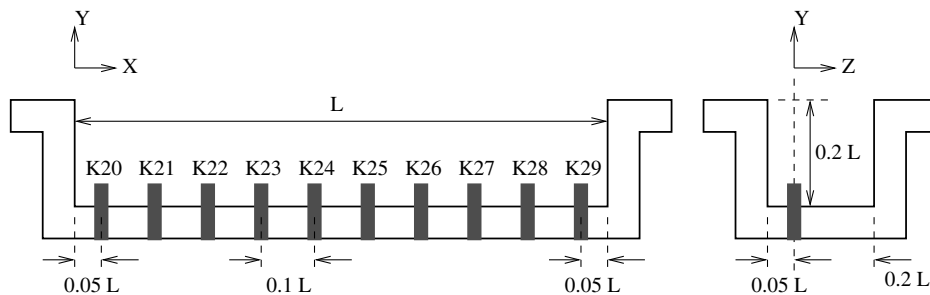
Peto [11,12], Ross [13], and Nightingale et al. [14] from QinetiQ are examples of campaigns that conducted a significant number of wind-tunnel experiments on cavities of several configurations over a broad range of Mach and Reynolds numbers. Tracy et al. [8] experimentally investigated acoustic-tone generation under transonic and subsonic conditions, with the results showing that Mach number had a large effect, and so the cavity-flow type cannot be reliably assessed on cavity geometry alone. However, it was also

found that the sound pressure spectrum-level (SPL) spectra were little affected by varying the Reynolds number.

Recent experimental endeavors have exploited nonintrusive optical techniques such as schlieren photography and optical reflectometry to study cavity flows. More advanced nonintrusive methods such as particle image velocimetry and laser Doppler velocimetry [15] are also beginning to appear in cavity-flow studies as a means of obtaining high-fidelity, high-resolution data. Such methods are, however, expensive and time-consuming, and so they are usually restricted to small-scale wind-tunnel tests. A summary of selected experimental clean-cavity studies can be found in Table 1.

Tables 2 and 3 contain a summary of selected passive-control studies. Leading-edge flow control devices attempt to reduce cavity noise and fluctuating pressure levels by reducing the interaction of the shear layer with the aft wall. Rossiter [7] found that leading-edge flat spoilers could reduce the intensity of the pressure fluctuations, but only for subsonic speeds. However, Shaw et al. [16] tested a leading-edge sawtooth spoiler and found that at Mach number 0.9 it reduced the amplitude of the broadband noise but did not affect the magnitude of the modes. Ukeiley et al. [26] found that the reduction inside the cavity was less than on the aft wall, implying that the main effect of the spoiler was indeed to minimize the shear-layer interaction with the aft cavity wall. However, lifting the shear layer into the freestream did not minimize the fluctuating pressure levels [26].

Another popular leading-edge control device is the transverse rod. Smith et al. [25], Ross and Peto [11,12], and Ukeiley et al. [26] investigated a variety of sizes and locations of rods. The studies concluded that virtually any size rod can function effectively; however, rods at the leading edge provide the greatest suppression and, in general, larger-diameter rods work best. However, the exact mechanism causing the suppression is not known, although for larger rods, the blockage effect could have been partly responsible. For smaller rods, the interaction of shed vortices with resonant behavior in the cavity could have been the key mechanism.

**Fig. 1 Locations of the pressure transducers inside the cavity.**

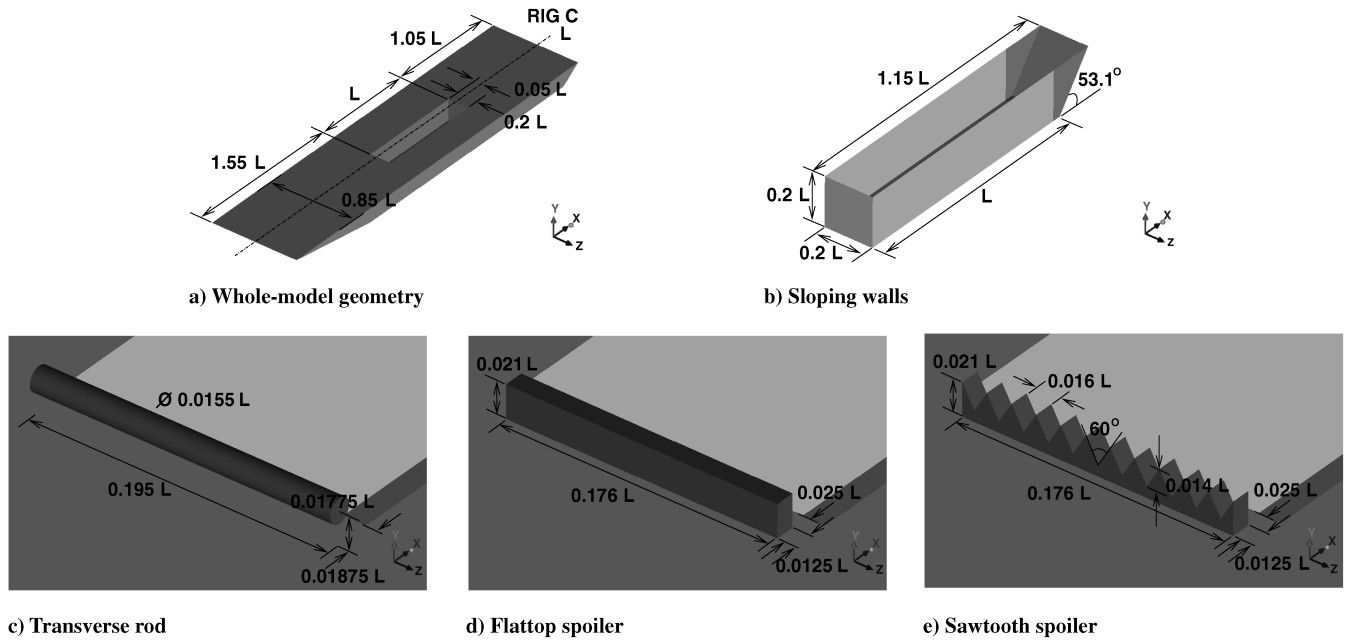


Fig. 2 Flow control devices used in combination with the clean cavity. All dimensions shown are nondimensionalized using the cavity length  $L$ .

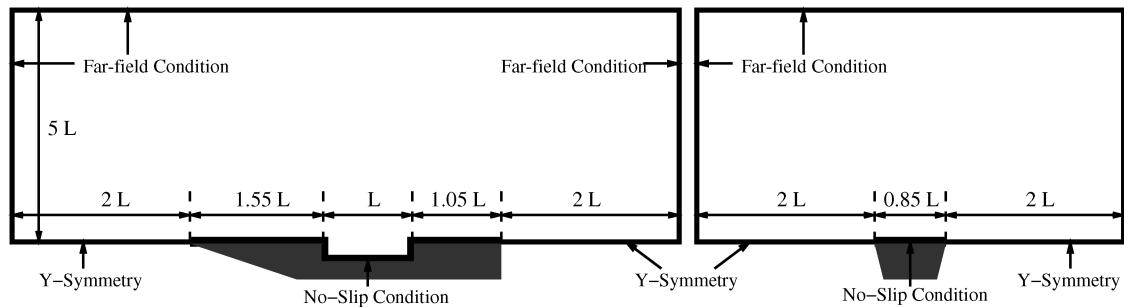


Fig. 3 Domain of the CFD grid and the boundary conditions on the surfaces.

## B. Review of Selected Computational Fluid Dynamics Studies

Early studies of cavity flows using computational fluid dynamics (CFD) focused on the use of Reynolds-averaged Navier–Stokes (RANS) equations in conjunction with various turbulence closures. Most applications of unsteady RANS (URANS) to cavity flows have employed algebraic turbulence models, especially different versions of the Baldwin–Lomax models [31], due to their simplicity [32,33]. However, such simple eddy viscosity models are not able to predict the turbulent cavity-flow field [34], and investigations with more advanced turbulence models such as the two-equation  $k-\varepsilon$  and  $k-\omega$  models were made. Most references to cavity-flow modeling with two-equation models were related to supersonic flow conditions [35,36], whereas applications of two-equation models to transonic cavity flows are rare. A detailed survey of published works on cavity flow can be found in [2].

One of the major drawbacks of URANS is its inherent inability to predict the full spectrum of turbulent scales. URANS models tend to well predict the larger scales associated with the lower-frequency discrete acoustic tones but fail to provide the same accuracy in

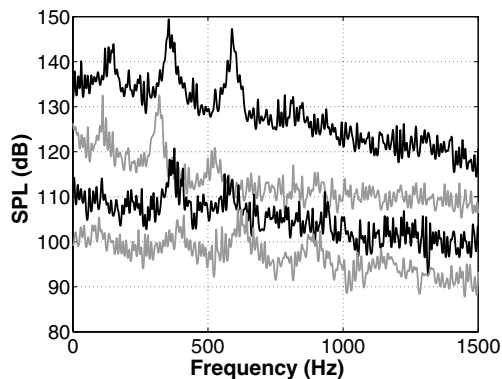
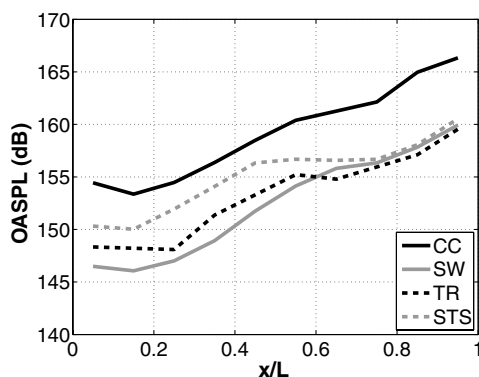
capturing the smaller, higher-frequency, and more intermittent time scales. The broadband noise is not captured by these models either. The presence of these multiple acoustic tones and of a large number of turbulent scales may mean that achieving a good level of accuracy and consistency with turbulence modeling is difficult for cavity flows.

More recent works have therefore used large-eddy simulation (Rizzetta and Visbal [37], Larchevêque et al. [38–40], and Nayyar et al. [41]) and detached-eddy simulation (Hamed et al. [42,43], Mendonça et al. [44] and Nayyar et al. [41]) to study the viability of using these techniques for the cavity-flow problem. Larchevêque et al. [39], Mendonça et al. [44], and Nayyar et al. [41] studied cavities with an  $L/D$  ratio of 5 and compared the results with experimental data from the M219 cavity [14]. Both large-eddy simulation (LES) and detached-eddy simulation (DES) models were found to perform better than URANS. A selection of clean-cavity CFD studies is summarized in Table 4.

As with the clean-cavity computations, numerical studies with passive flow control began with using URANS and then progressed

Table 6 Details of the grids used in the computations

Case	Number of blocks		Number of grid points		
	Cavity	Total	Cavity	Control device	Total
Clean cavity	64	256	$0.5 \times 10^6$	N/A	$2.2 \times 10^6$
Slanted aft wall	160	724	$1.4 \times 10^6$	$0.2 \times 10^6$	$5.1 \times 10^6$
LE transverse rod	160	1032	$1.4 \times 10^6$	$0.3 \times 10^6$	$5.8 \times 10^6$
LE flat spoiler	160	1010	$1.4 \times 10^6$	$0.2 \times 10^6$	$5.5 \times 10^6$

a) PSD for kulite K29 -  $x/L=0.95$ 

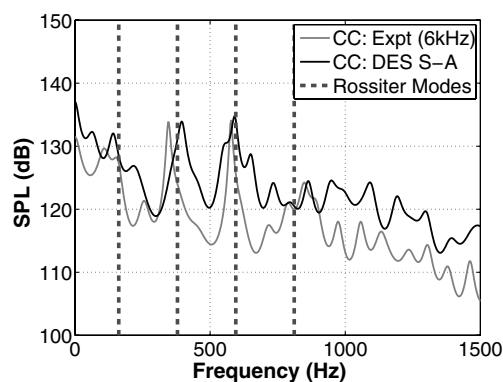
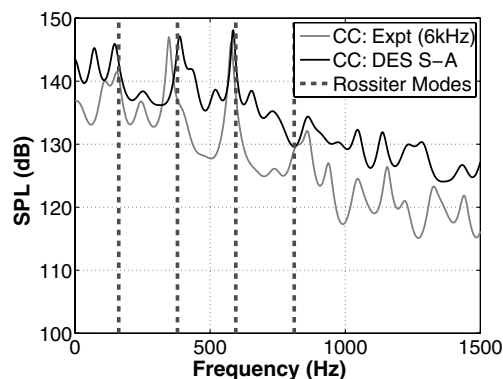
b) OASPL along cavity floor

**Fig. 4** PSD at the rear of the cavity and OASPL along the cavity floor for the experimental clean cavity (CC), SW, TR, and STS. In the PSD plot, the curves are separated by introducing offsets and are in the same order as the legend in the OASPL. From the top, CC (unaltered), SW ( $-10$  dB), TR ( $-20$  dB), and STS ( $-30$  dB).

to methods such as LES and DES (Tables 2 and 3). Baysal et al. [27] performed two-dimensional computational analysis on transonic turbulent cavities using URANS equations with the Baldwin–Lomax turbulent model [31]. Two flow control methods were studied: slanted aft wall and a leading-edge flattop spoiler. Although both suppression methods reduced peak tones, neither reduced the levels of the broadband contribution. Arunajatesan et al. [28] used a hybrid RANS-LES method to study a transverse rod deployed at the lip of the cavity. The rod lifted the shear layer, which no longer impinged on the aft wall. The lifting was driven by the gap between the rod and front wall, which caused the flow to accelerate, resulting in an asymmetric shedding pattern. The reduced loading was not just limited to the aft wall, but along the cavity floor as well. A similar study was performed by Comte et al. [29] on a deep cavity ( $L/D$  ratio of 0.42). LES and DES computations showed the increased level of turbulence due to the existence of the transverse rod; however, the LES results had a larger spectrum of small-scale vortices. It was thought that the von Kármán vortices produced by the rod energized and thickened the shear layer, making it less likely to break down and therefore span the entire cavity length.

### C. Outline of Present Investigation

In view of the preceding survey, this paper presents a set of results using DES for cavity flows with passive flow control. CFD results for cavities with a slanted aft wall and leading-edge spoilers are compared against the data set obtained by Nightingale et al. [14]. Suggestions regarding the flow mechanisms responsible for the effect of each flow control device investigated are then put forward. Although the devices studied here have been investigated before

a) Kulite K20 -  $x/L=0.05$ b) Kulite K29 -  $x/L=0.95$ 

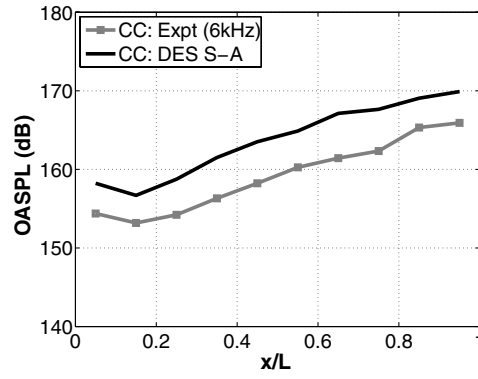
**Fig. 5** PSD plots at the front and rear of the cavity for the clean-cavity configuration.

(either experimentally or numerically), this is the first in-depth comparison of several passive-control methods with the aim of clearly identifying the mechanisms responsible for acoustic suppression and the effects of the devices on the flowfield and the structure of the cavity.

The rest of the paper is organized as follows: A description of the experimental data available to validate the CFD results is presented in Sec. II. The employed numerical method and the details of the computations are discussed in Secs. III and IV, respectively. The CFD results are presented in Sec. V, which is split into several sections. The first compares the CFD results with the experimental data to validate the computations. Then the flowfields, wall forces, and acoustic field are analyzed to gain a complete picture of the suppression mechanisms for each device. Finally, Sec. VI draws conclusions from the study.

## II. Selection of Test Cases and Available Experimental Data

Pressure measurements were obtained from the Defence and Evaluation Research Agency (DERA) in Bedford, England, U.K. [14]. The DERA wind tunnel was a 9 by 8 ft continuous-flow transonic wind tunnel with a ventilated roof, floor, and side walls. The generic cavity rig model was positioned at zero pitch and yaw angle to the freestream flow, which had a Mach number of 0.85 and, depending on the configuration, Reynolds numbers between  $4 \times 10^6$  and  $6.5 \times 10^6$  based on the cavity length. The cavity model was designed to represent a range of geometries. For the  $L/D$  ratio of 5, the cavity had a length of 20 in. and a width and depth of 4 in. Unsteady pressure measurements were recorded inside the cavity via pressure transducers, which, for most cases, were sampled at a rate of 6 kHz for approximately 3.5 s. Additional tests were conducted using a sampling rate of 31.25 kHz for a small number of cases. Table 5 shows the locations of the pressure transducers in the cavity non-



a) OASPL

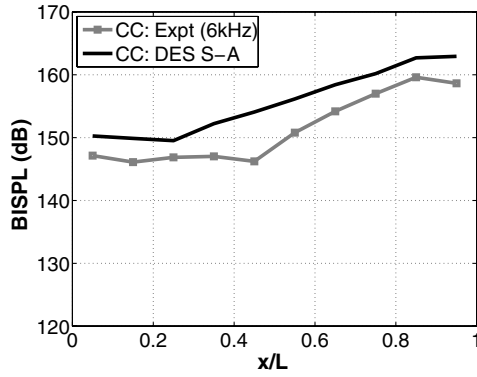
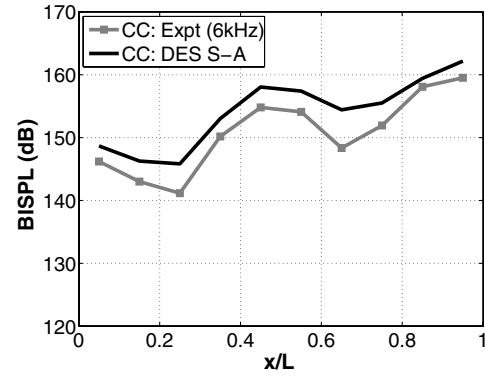
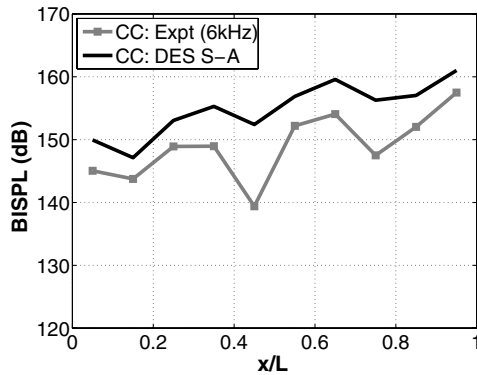
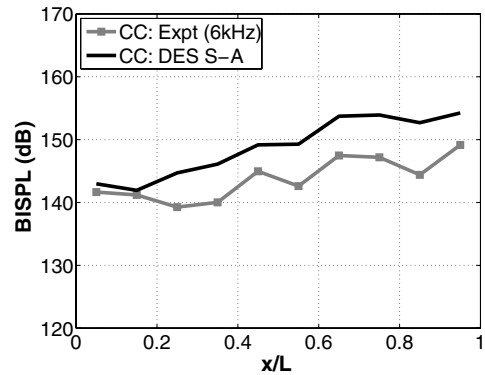
b)  $50 \leq f \leq 250$  Hzc)  $250 \leq f \leq 450$  Hzd)  $500 \leq f \leq 700$  Hze)  $700 \leq f \leq 900$  Hz

Fig. 6 OASPL and BISPLs along the cavity floor for the clean-cavity configuration.

dimensionalized using the cavity length. Various configurations of pressure transducers were used for each test case; however, the main 10 transducers used for comparisons with the data were located on the cavity floor (designated as K20–K29 and shown in Fig. 1) and were common for all test cases.

Four different types of passive flow control devices were used during the experiments (Fig. 2): slanted walls (SW), leading-edge transverse rod (TR), leading-edge flattop spoiler (FTS), and leading-edge sawtooth spoiler (STS). For the slanted-wall cases, the fore and aft walls could be angled at 53.1, 63.4, and 76.0 deg to the horizontal. The transverse rod had a diameter of 0.31 in., with the center of the rod being 0.375 in. upstream of the front edge of the cavity. The flat and sawtooth spoilers were 0.25 in. upstream of the front cavity edge and 0.42 in. in height, which was approximately equal to the height of the boundary layer of the clean-cavity configuration at that location.

### III. Numerical Methods

#### A. Governing Equations

The parallel multiblock flow solver has been successfully applied to a variety of problems, including cavity flows, hypersonic film cooling, spiked bodies, flutter, and delta-wing flows, among others [49]. The governing equations are the unsteady three-dimensional compressible Navier–Stokes equations, written in dimensionless form as

$$\frac{\partial Q}{\partial t} + \frac{\partial}{\partial x} \left( F^{\text{inv}} + \frac{1}{Re} F^{\text{vis}} \right) + \frac{\partial}{\partial y} \left( G^{\text{inv}} + \frac{1}{Re} G^{\text{vis}} \right) + \frac{\partial}{\partial z} \left( H^{\text{inv}} + \frac{1}{Re} H^{\text{vis}} \right) = S \quad (1)$$

where  $Q$  contains the unsteady terms and  $F$ ,  $G$ , and  $H$  are spatial flux

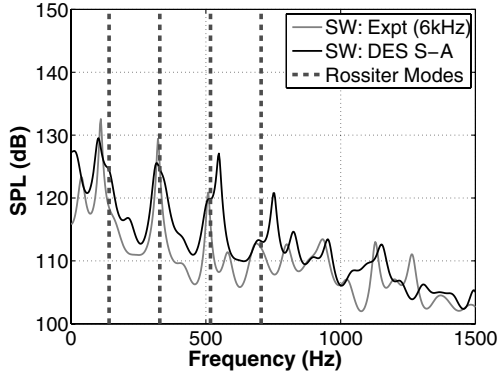
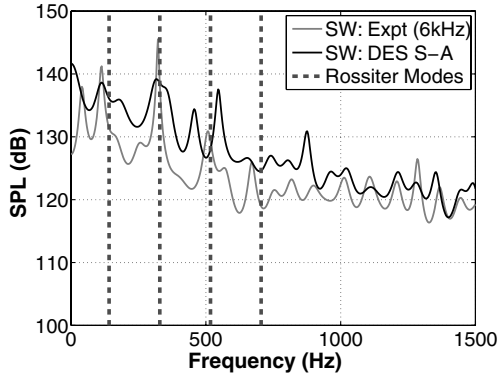
a) Kulite K20 -  $x/L=0.05$ b) Kulite K29 -  $x/L=0.95$ 

Fig. 7 PSD plots at the front and rear of the cavity for the 53 deg slanted-aft-wall configuration.

vectors and have been split into their inviscid (inv) and viscous (vis) parts. The source vector is denoted by  $\mathbf{S}$ .

The code solves the governing equations on multiblock structured grids using a cell-centered finite volume method. The convective terms are discretized using either Osher's or Roe's scheme. MUSCL interpolation is used to provide formally third-order accuracy, and the Van Albada limiter is used to avoid spurious oscillations across shocks. The time-marching of the solution is based on an implicit dual-time-stepping method. The final algebraic system of equations is solved using a conjugate gradient method in conjunction with block incomplete lower-upper factorization. A number of turbulence models, including one- and two-equation statistical models as well as LES and DES formulations, have been implemented into the code. More details of the employed CFD solver and turbulence models are given by Nayyar et al. [41]. For the work presented in this paper, DES was employed along with the Spalart-Allmaras (S-A) turbulence model [50].

## B. Proper Orthogonal Decomposition

Proper orthogonal decomposition (POD) is a mathematical technique used in many applications, including image processing, signal analysis, and data compression [51]. It aims to obtain low-dimensional approximate descriptions of high-dimensional processes [52], therefore eliminating information that has little impact on the overall process. It was first introduced by Lumley [53] in the context of fluid mechanics and turbulence, to decompose the flow into modes. These modes identify the large coherent structures that contribute to the flow. However, many applications of POD use the method of snapshots, which was introduced by Sirovich [54], for highly spatial resolved data. The snapshots are usually taken at instances in time so that various states of the flowfield are represented. Using the scalar-valued method of snapshots [55], any flow variable ( $u(x, t)$ ) within a snapshot can be expanded in terms of spatial modes  $\Phi_i(x)$  and temporal eigenfunctions  $a_i(t)$ :

$$u(x, t) = u_m(x) + \sum_{i=1}^N a_i(t) \Phi_i(x) \quad (2)$$

where  $u_m(x)$  is the mean quantity.

The eigenvalues from the decomposition  $\lambda_i$  are representative of the amount of energy stored in each mode from the flow. A nominal criterion, given by Sirovich [54], is that the number of retained  $n$  should be equivalent to 99% of the energy:

$$\sum_{i=1}^n \lambda_i / \sum_{i=1}^N \lambda_i > 0.99 \quad (3)$$

However, application of this method to cavity-flow problems has shown that far less modes were needed to reconstruct the flowfield, with the resultant energy captured closer to 70% [45,56,57]. With this in mind, the initial investigation into the method was performed with the view of using it as a form of data compression. If only a few modes needed to be stored, then the level of data compression would be far greater than any lossless methods currently available [57]. This meant that the POD was applied only as a postprocessing step, in which low-order reconstructions were gained from snapshots of the full-order system. Although the snapshots are usually taken at key states of the flowfield, the flow over a cavity is extremely complex and contains frequencies over a broad range. Therefore, snapshots were taken at regular intervals in the flow over a time period equal to one period of the lowest Rossiter mode ( $T_{\text{Rossiter}1}$ ).

## IV. Details of Computations

The flow domain used for computations is shown in Fig. 3, along with the applied boundary conditions. The cavity was modeled on the experimental setup (Fig. 2a), with all solid surfaces having no-slip boundary conditions. The values at the far field were extrapolated, and so the far-field boundaries had to be set a large distance away from the cavity. Therefore, the domain extended five cavity lengths above the surface of the plate and an extra two cavity lengths around the plate on each side. The boundary conditions for extra section around the plate were set to  $Y$  symmetry, which imposed a slip condition so that no boundary layer would build up. Grids of up to 6 million cells were used, with approximately 25% of the points located within the cavity.

Three passive-control cases were computed: 53 deg slanted aft wall, leading-edge transverse rod, and leading-edge flat spoiler. For the cases in which leading-edge devices were present, the region near the front of the cavity had to be refined so that spoilers could be embedded in the grid. The details of the grids can be found in Table 6.

The DES computations had a time step of  $1.84 \times 10^{-6}$  s, which was needed to resolve high frequencies in the flow. The time step equated to a frequency of 543 kHz, and so according to the Nyquist theorem, the highest frequency that was accurately resolved by the computation was 272 kHz. The Nyquist theorem then needs to be applied again for sampling the data, and so the highest-possible sampling frequency that could be used to gain unsteady pressure measurements from the flow was 136 kHz. Further, all of the numerical data were down-sampled to match the sampling frequency of the experimental data. For each computation, the total runtime was 0.12 s, apart from the clean cavity, which was run for 0.17 s. The first 0.02 s ( $3 \times T_{\text{Rossiter}1}$ ) were discarded, and so this gave each computation approximately 0.1 s ( $15 \times T_{\text{Rossiter}1}$ ) of data.

For all cases computed, the Mach number at the freestream ahead of the cavity was kept at 0.85 and the Reynolds number based on the length of the cavity was  $1 \times 10^6$ . The Reynolds number was initially reduced to allow for efficient computations using LES. However, it has been shown that reducing the Reynolds number down from  $6.5 \times 10^6$  to  $1 \times 10^6$  had little effect on the cavity-flow field [2]. The recent results were kept at this lower Reynolds number, not only so they could be compared with the clean-cavity data, but also because the experimental results for different flow control devices were not all performed at the same Reynolds number. Therefore, it was kept at the lower value for consistency. As with the

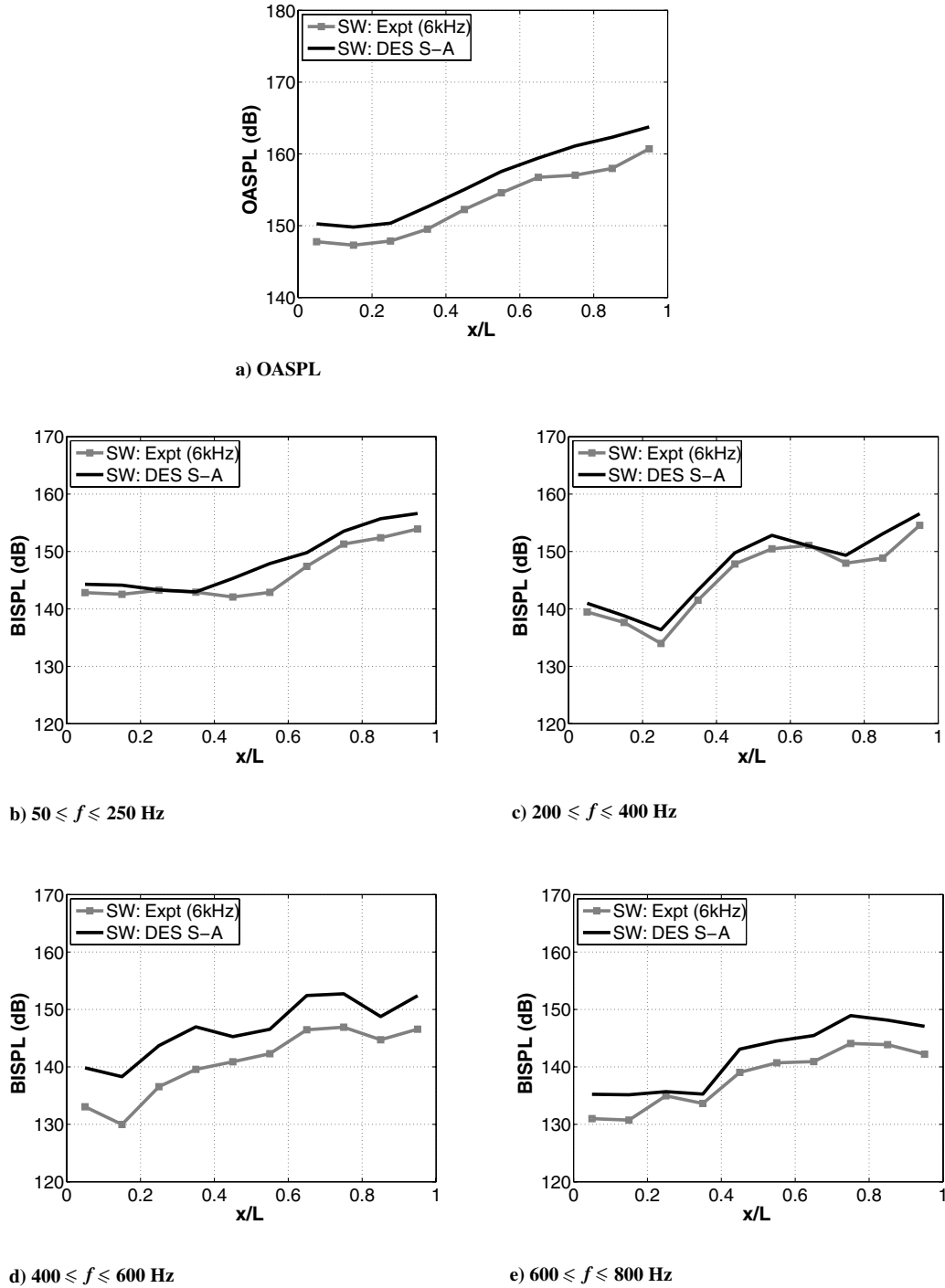


Fig. 8 OASPL and BISPLs along the cavity floor for the 53 deg slanted-aft-wall configuration.

experimental setup, the plate was angled at zero pitch and yaw to the freestream flow in the CFD computations.

## V. Results and Discussion

First, spectral analyses are performed and compared with the experimental data described in Section II to validate the computations and assess the level of noise suppression for each method. Second, flowfield visualizations will be used to determine how each method achieves the noise suppression.

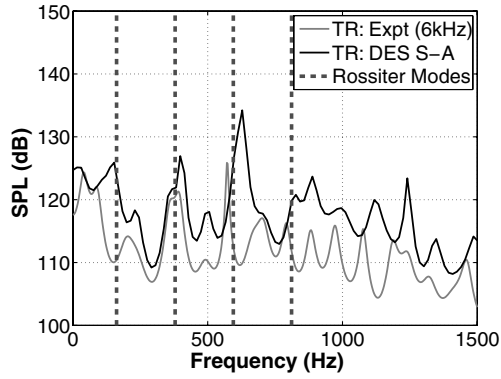
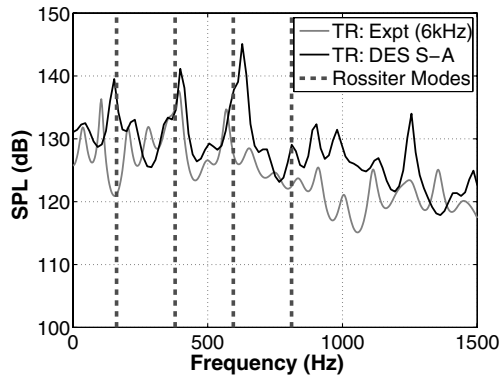
### A. Spectral Analyses

Power spectral density (PSD) and overall sound pressure levels (OASPL) were computed along the cavity floor for each test

case. The PSD is based upon the unsteady pressure  $p'$ , where  $p' = p - p_m$ . The PSD was calculated using the Burg estimator [58], as it produces better resolved peaks for short signals than traditional Fourier transforms [39]. The length of the time signal gave a frequency resolution of 10 Hz. The experimental signal was shortened to the same length as the numerical signal and processed using the same method. For a description of the PSD in terms of decibels, the natural definition is that of the SPL [59]:

$$\text{SPL}(f) = 10 \log \left( \frac{\text{PSD}(f) \Delta f_{\text{ref}}}{p_{\text{ref}}^2} \right) \quad (4)$$

where  $\Delta f_{\text{ref}}$  is a reference frequency, usually set to 1 Hz, and

a) Kulite K20 -  $x/L=0.05$ b) Kulite K29 -  $x/L=0.95$ 

**Fig. 9** PSD plots at the front and rear of the cavity for the leading-edge transverse rod configuration.

$p_{\text{ref}}$  is the international standard for the minimum audible sound, which has the value of  $2 \times 10^{-5}$  Pa [59].

The variation in pressure levels along the cavity floor was studied using the root mean square of the unsteady pressure,  $p'_{\text{rms}}$ , and can be obtained from the measurements using the following equation:

$$p'_{\text{rms}} = \sqrt{\frac{1}{N} \sum (p')^2} \quad (5)$$

Although  $p'_{\text{rms}}$  is measured in pascals (or any other unit of pressure), it is customary to report it as the OASPL [39,41,48,59]:

$$\text{OASPL} = 20 \log(p'_{\text{rms}}/p_{\text{ref}}) \quad (6)$$

Band-integrated SPL (BISPL) plots are also presented, which show the energy content within a particular frequency range. This aids in identifying which frequencies are significant. The shape of each banded mode is also important, as it represents how each frequency band varies along the cavity length. For each test case, four frequency ranges are plotted that encompass the first four Rossiter modes.

### 1. Summary of Experimental Data

Figure 4 shows the PSD at the rear of the cavity and the OASPL along the cavity floor. The clean-cavity configuration is compared with three of the control devices tested. At present, the data for the flattop spoiler are not available. In the PSD plots for experimental clean-cavity data, three tones can clearly be seen: the first located at a frequency of about 140 Hz, the second at 360 Hz, and the third at around 590 Hz. A fourth, much weaker, tone can be seen at 785 Hz. The PSD also shows that the magnitudes of the tones were reduced by the control devices; however, none of the modes were completely suppressed by any of the devices tested. Also, tones for the slanted aft wall shifted to slightly lower frequencies, whereas the tones for the

leading-edge devices shifted to slightly higher frequencies. The OASPL along the cavity floor shows that all three devices produced noise reductions, although the slanted aft wall was more effective at the front of the cavity than the leading-edge devices.

### 2. Cavities Without Flow Control

Comparisons of the numerical and experimental data for the clean cavity (Fig. 5) revealed some discrepancies, although all the tones present in the experiments were also present in the CFD. At the front of the cavity, the DES overpredicted the magnitude of the first three tones. Also, the frequency of the first tone was slightly underpredicted and there was a small overprediction of the second tone. At the rear of the cavity, the DES results overpredicted the magnitude of the broadband noise and so the tones were not as prominent as in the experimental data, although it is still apparent that the magnitudes of the first three tones were overpredicted. As with the spectra at the front of the cavity, the frequency of the third tone was correctly predicted, with the first and second tones being slightly under- and overpredicted, respectively, in comparison with the experimental data.

The OASPL and the BISPL plots (Fig. 6) show that the magnitudes of all of the modes were overpredicted, with the largest overprediction occurring in the third band. However, all four curves of the DES predictions resemble those of the experimental data, suggesting that the flow structures inside the cavity were well predicted.

### 3. Cavities with Trailing-Edge Devices

Figure 7 presents the PSD of the cavity with the aft wall slanted at 53 deg to the horizontal. At the front of the cavity, the frequencies of the dominant first and second tones were well predicted in comparison with the experiments. The magnitudes were also well predicted, although both tones had a slight underprediction. The frequency and magnitude of the third tone were both overpredicted. The same trends can be seen at the rear of the cavity. Because of the slanting of the rear wall, the length of the cavity at the mouth was longer than on the floor, and so the frequencies of the Rossiter modes shifted down to lower values. This was reflected in the tones of the experimental data, as they were very close to the predictions of Rossiter's formula. It also shows that the DES correctly predicted the shift of the tones. Finally, the level of the broadband noise compared favorably with the experimental data.

The overpredictions for the slanted aft wall were reflected in the SPLs along the cavity floor, which are shown in Fig. 8. The OASPL is shown in Fig. 8a, which shows that the levels were overpredicted by between 2 and 4 dB. However, the shape of the curve was well predicted compared with that of the experimental data, again indicating that the flow structures inside the cavity were well resolved. This is also shown in the banded frequency plots in Figs. 8b–8d. The magnitudes of the first and second bands were generally well predicted, with the largest overprediction coming from the third mode, which was consistent with the DES results from the clean-cavity case.

### 4. Cavities with Leading-Edge Devices

The PSD for the transverse rod (Fig. 9) showed similar trends to the previous two cases. The first three modes at both the front and the rear of the cavity were overpredicted compared with the experimental data in both frequency and magnitude. The third mode differed the most, with levels overpredicted by 8–10 dB. The consequence of the overprediction was that the third tone was dominant.

Figure 10a shows that the effect of overpredicting the third tone results in an overprediction of 7–8 dB in OASPL, all along the cavity length. In the BISPL plots, differences between the experimental and the numerical data at the front of the cavity can be seen in the first and second modes; however, the shapes of the other modes were, in general, very similar to those of the experimental data.

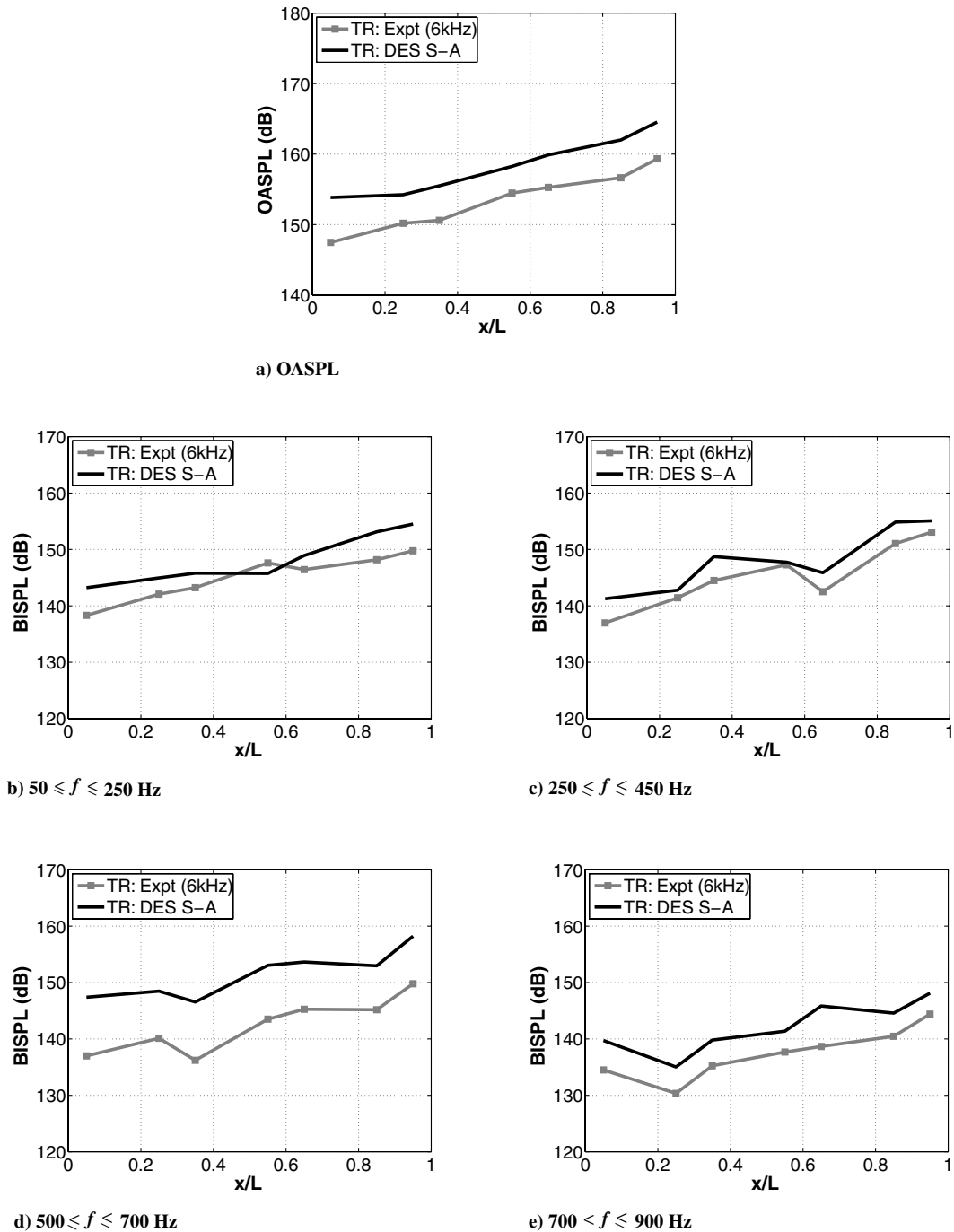


Fig. 10 OASPL and BISPLs along the cavity floor for the leading-edge transverse rod configuration.

The numerical results from the flat spoiler are compared against the experimental results of the sawtooth spoiler, as data for the flat spoiler were not available. The sawtooth spoiler has the same overall dimensions and is located in the same position as the flat spoiler, and so the data are only provided to give a general indication of the effect of a leading-edge spoiler. It can be seen that the PSD for flattop spoiler (Fig. 11) contains a higher number of tones, making identifying the Rossiter modes more difficult. At the front of the cavity, tones appear at similar frequencies to the experimental sawtooth spoiler data, especially around the first and third Rossiter modes. However, comparisons and identifying Rossiter modes at the rear of the cavity were much more difficult. The OASPL (Fig. 12a) showed that the shape for the two data sets was similar, with the numerical SPL 4–6 dB higher than the experiments. As with the PSD plots, the shapes of the banded modes (Figs. 12b–12e) had some similarity with the experimental data close to the front of the cavity, but differed downstream, suggesting that the

sawtooth spoiler had a different effect on the flowfield to the flattop spoiler.

It should also be noticed that the structure of the BISPL plots for both leading-edge devices differed from those of the clean cavity and the slanted aft wall. In both the experimental and numerical data, the  $W$  structure that was observed in the second tones in the clean cavity and the slanted-aft-wall cases was not apparent at all.

##### 5. Summary of Spectral Analyses

In all four preceding cases, the DES overpredicted the magnitude of the pressure fluctuations compared with the experimental data. These overpredictions have been seen in many recent LES and DES CFD studies [30,39,40,47,48,60], and an overprediction of up to 5 dB is not uncommon.

One explanation for the differences between the experimental and CFD data is due to the short signal length of the CFD computations.

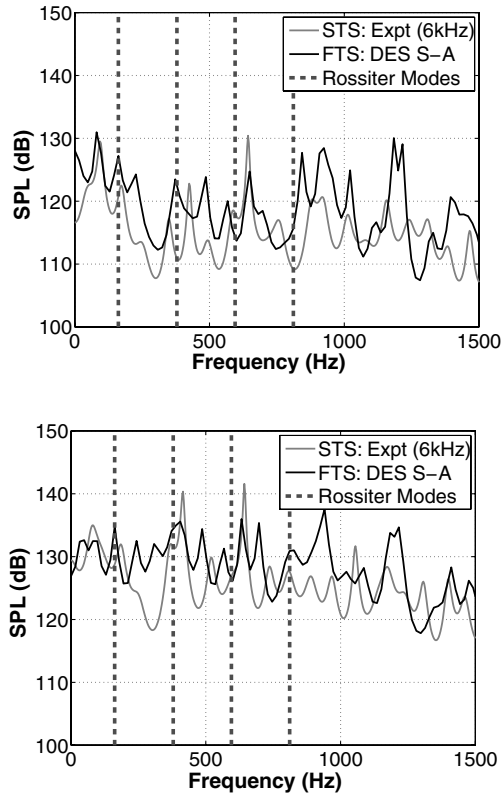


**Fig. 11** PSD plots at the front and rear of the cavity for the leading-edge flattop spoiler configuration.

The experimental signals can be as long as 30 s, which is not practical for complex CFD simulations. The experimental signals given earlier are shortened to the CFD signal length; however, the section of experimental signal used is the same in all cases. Larchevêque et al. [40] also divided up the experimental signal into sections equaling that of the numerical data, but then processed each one individually. It was found that errors of less than 2 dB can be gained between the spectra of the numerical data and the spectra of the section of experimental data that best resembled the numerical spectra.

Overall, the shapes of the OASPL and the BISPL curves were well predicted by the DES S-A model, suggesting that the physics inside the cavity was well predicted compared with the experimental data.

## B. Flowfield Analysis

### 1. Instantaneous and Time-Averaged Flowfields

Figure 13 shows contours of instantaneous Mach number for the clean cavity and the passive flow control devices. In the clean-cavity case, the shear layer started to break down after approximately one-third of the cavity length. The slanted aft wall did not delay the breakdown of the shear layer. However, the shear layer diffused less, as it can be seen that higher Mach numbers were more restricted to the shear layer. This also resulted in a lower Mach number across most of the aft wall.

Figure 13c shows that the presence of the transverse rod lifted the shear layer above the height of the cavity aft wall. It also showed that the breakdown of the shear layer was delayed until about two-thirds of the cavity length. This was due to the interaction between the vortices shed from the rod and the shear layer, which had a stabilizing effect. However, in the rear of the cavity, higher Mach numbers were observed than for the slanted aft wall. In fact, the Mach numbers were comparable with those seen in the clean-cavity configuration.

The flowfield in the flattop spoiler (Fig. 13d) case appeared much more unsteady than in any other case. The shear layer was deflected upward by the spoiler, but started to break down almost as soon as it separated from the top of the spoiler. Therefore, the level of

breakdown of the shear layer was actually higher than in the clean-cavity configuration. Again, high Mach numbers were seen in the rear half of the cavity; however, in the flattop spoiler case, higher Mach numbers were also seen in the front part of the cavity.

To identify structures within the flow, instantaneous isosurfaces of  $Q$  criteria are shown in Fig. 14. Hunt et al. [61] proposed the  $Q$  criterion to identify vortex cores and defined it as the positive second invariant of the velocity gradient tensor  $\nabla u$ , with the additional condition that the pressure must be lower than the ambient value. The second invariant of  $Q$  is defined as

$$Q \equiv \frac{1}{2}(u_{i,i}^2 - u_{i,j}u_{j,i}) = -\frac{1}{2}(u_{i,j}u_{j,i}) = \frac{1}{2}(\|\boldsymbol{\Omega}\|^2 + \|\mathbf{S}\|^2) \quad (7)$$

where  $\mathbf{S}$  and  $\boldsymbol{\Omega}$  are the symmetric and antisymmetric components of the  $\nabla u$ . Thus, the  $Q$  criteria represent the local balance between shear strain rate and vorticity magnitude [62].

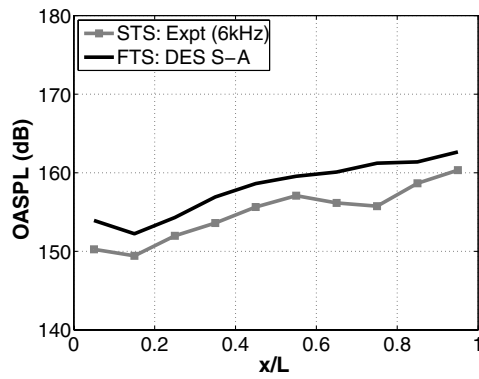
It can be seen from Fig. 14 that the clean cavity was characterized by large structures emanating from the breakdown of the shear layer. These structures occupied the latter two-thirds of the cavity and interact with the aft wall. The structures inside the cavity for the controlled cases were generally smaller in size than those in the clean cavity, although the presence of the leading-edge devices created large structures within the shear layer. It seemed that the two devices had a different effect on the shear layer. As noticed in the Mach contours, the structures from the transverse rod had a stabilizing effect. The spanwise structures shed from the rod were broken up and turned into streamwise structures by the freestream flow about halfway along the cavity length. The shear layer then seemed to break down after the structure of the spanwise vortices was lost. The shear layer for the flat spoiler seemed to have more small structures than any other case.

Time-averaged contours of  $Q$  criteria are shown in Fig. 15, in which it can be seen that the isosurfaces for the clean cavity and the slanted aft wall had similar characteristics. The most prominent structures were seen at the trailing-edge of the cavity, inside the vertical edges. However, these structures were not seen in the leading-edge devices, in which the shear layer was lifted above the aft wall. Large structures were also seen along the side walls in the clean-cavity case, which shows that the shear layer was not confined to the width of the cavity. Similar structures can be seen in the controlled cases, although these were much smaller in size and more numerous in the cases with the leading-edge devices.

Mean longitudinal velocity profiles were taken at various distances across the cavity to see the behavior of the shear layer for each of the control devices (Fig. 16). At the first station ( $x/L = 0.1$ ), the clean cavity and slanted wall had very similar profiles. Both the leading-edge devices immediately lifted the shear layer above the cavity line of the cavity mouth. Downstream, it can be seen that the flat spoiler lifted the shear layer higher into the freestream flow than the transverse rod, although as noticed in the instantaneous flowfields, the level of breakdown of the shear layer was also higher. At the midpoint of the cavity, the shear layer for the flat spoiler had diffused to a much larger extent than for the transverse rod. Also, the shear layer for the slanted aft wall did not break down as much as for the clean cavity.

### 2. Acoustic Field

Although the noise inside the cavity is important, another point of interest is how noise is propagated out of the cavity. Figure 17 shows contours of instantaneous dilatation ( $\nabla \cdot u$ ) at the cavity centerline. Although the mesh surrounding the cavity was not designed for an in-depth analysis of acoustic propagation, some conclusions can be drawn on the effects of the control devices, because similar grid densities were used for all cases. It can be seen that for the clean-cavity case (Fig. 17a), strong acoustic waves were observed. The structures in the shear layer travel toward the aft wall, whereas outside the cavity, reflected acoustic waves travel out of the cavity and back toward the front wall. In the slanted-aft-wall case (Fig. 17b), the reflected acoustic waves in the far field still existed; however, they were much weaker than those observed in the clean-cavity



a) OASPL

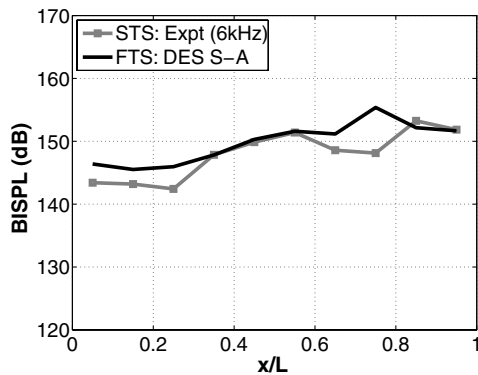
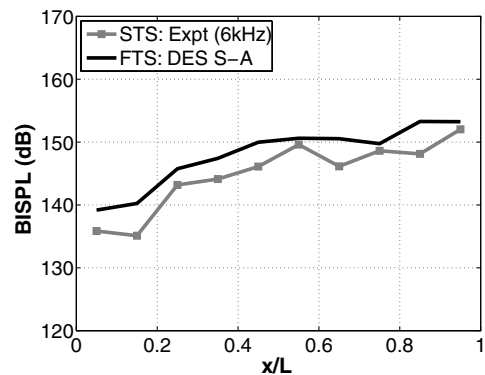
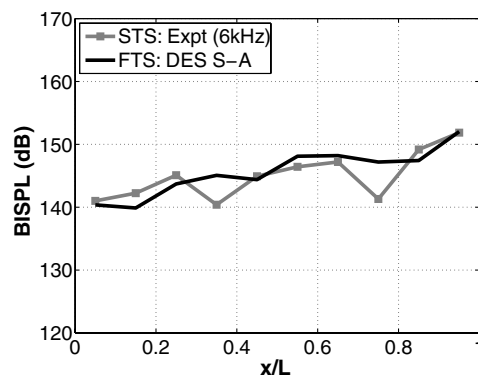
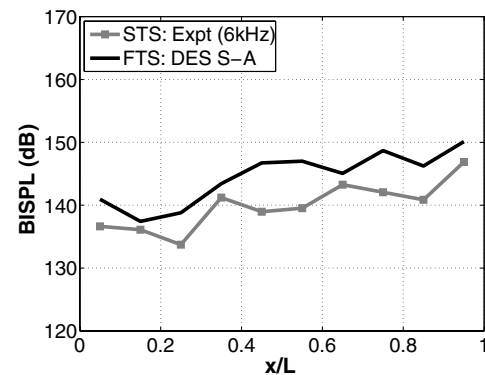
b)  $50 \leq f \leq 250$  Hzc)  $250 \leq f \leq 450$  Hzd)  $500 \leq f \leq 700$  Hze)  $700 \leq f \leq 900$  Hz

Fig. 12 OASPL and BISPLs along the cavity floor for the leading-edge flattop spoiler configuration.

configuration. It can also be seen that the structures inside the cavity were more confined to areas around the shear layer than for the clean cavity.

The presence of the transverse rod had a significant effect on the acoustic field, both inside and outside the cavity (Fig. 17c). It can be seen that, due to the lifting of the shear layer off the aft wall, the waves propagating outside the cavity into the far field were greatly reduced. It was noted from the instantaneous Mach contours that the vortices shed from the rod aided in stabilizing the shear layer; however, it looked as though this also resulted in more unsteadiness within the cavity, especially close to the front wall. Strong acoustic waves can also be seen emanating from the rod at the front of the cavity.

As with the transverse rod case, high levels of unsteadiness can be seen throughout the cavity for the flattop spoiler case (Fig. 17d), although the levels at the front of the cavity were even higher than for the transverse rod. Again, the lifting of the shear layer also reduced

the strong acoustic waves propagating into the far field, although small acoustic waves were seen outside the cavity as a result of the increased breakdown of the shear layer and from reflections off the spoiler.

Figure 18 shows isosurfaces of the instantaneous unsteady pressure, with isosurface values representing 100 dB. This highlights the large structures that are created in the clean-cavity configuration by the interaction of the shear layer on the aft wall. The three controlled cases still contained large flow structures, but these were confined inside the cavity and the regions near the shear layer.

OASPL distributions throughout the computational domain (Fig. 19) provided further evidence of the effects of the control devices. The decrease in OASPL that was gained from slanting the aft wall can be seen both inside and outside the cavity. The region of high OASPL in the rear of the cavity was decreased to a small area in which the shear layer impacted the aft wall. Similar shapes in the OASPL distribution between the clean cavity and the slanted aft wall

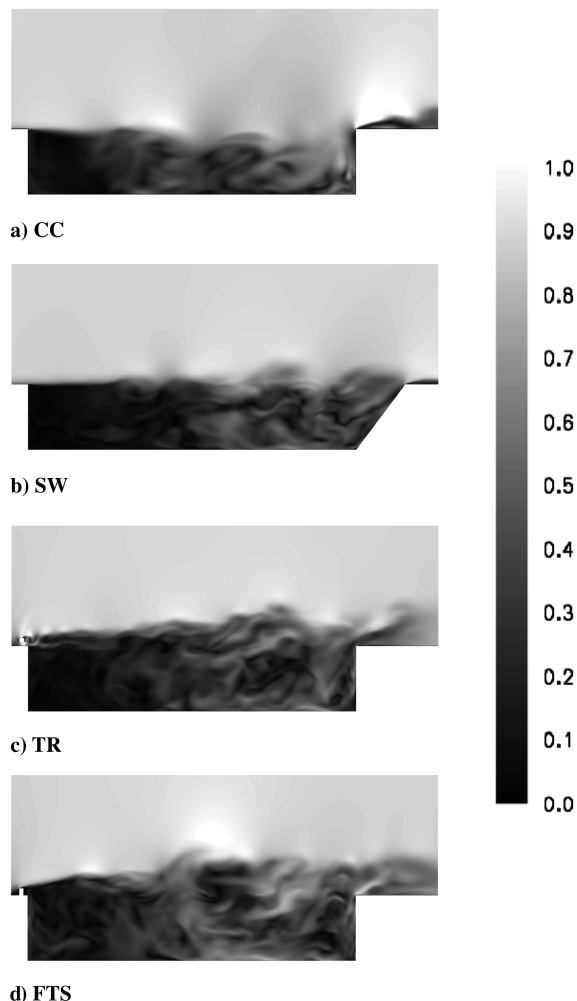


**Fig. 13** Instantaneous Mach contours at the cavity centerline for the clean-cavity and the passive flow control devices. All plots at time,  $t = 0.06166$  s.

can be seen, although all of the levels in the latter case were lower. Also, less noise was propagated out of the cavity, with levels almost 10 dB lower at a distance of one cavity length above the cavity mouth.

The transverse rod reduced the OASPLs inside and outside the cavity (Fig. 19c). The area of high OASPL on the aft wall for the clean-cavity configuration was not apparent on the controlled case. The main effect, however, was seen outside the cavity. Because the acoustic pressure waves were greatly reduced, the OASPL did not propagate away from the cavity. Therefore, it can be seen that at any point in the far field, the OASPL was approximately 15 dB less in the controlled case.

The OASPL distribution for the flattop spoiler (Fig. 19d) shows higher levels in front of the spoiler, which were caused by reflections from the impact of the boundary layer of the front of the spoiler. Inside the cavity, there were many similarities with the transverse rod, although higher levels were seen in the shear layer in the middle of the cavity. Also, the contour lines were slightly shifted toward the front of the cavity. Outside the cavity, similar noise levels were seen as for the transverse rod.

### C. Wall Forces

To gain an insight into the forces exerted on the cavity by the flow, the force on each wall was studied. This was carried out by integrating the pressure over the wall area  $A$  and then converted to a force coefficient  $C_F$ :

$$C_F = \frac{1}{q_\infty A} \iint_{\text{wall}} p dS \quad (8)$$

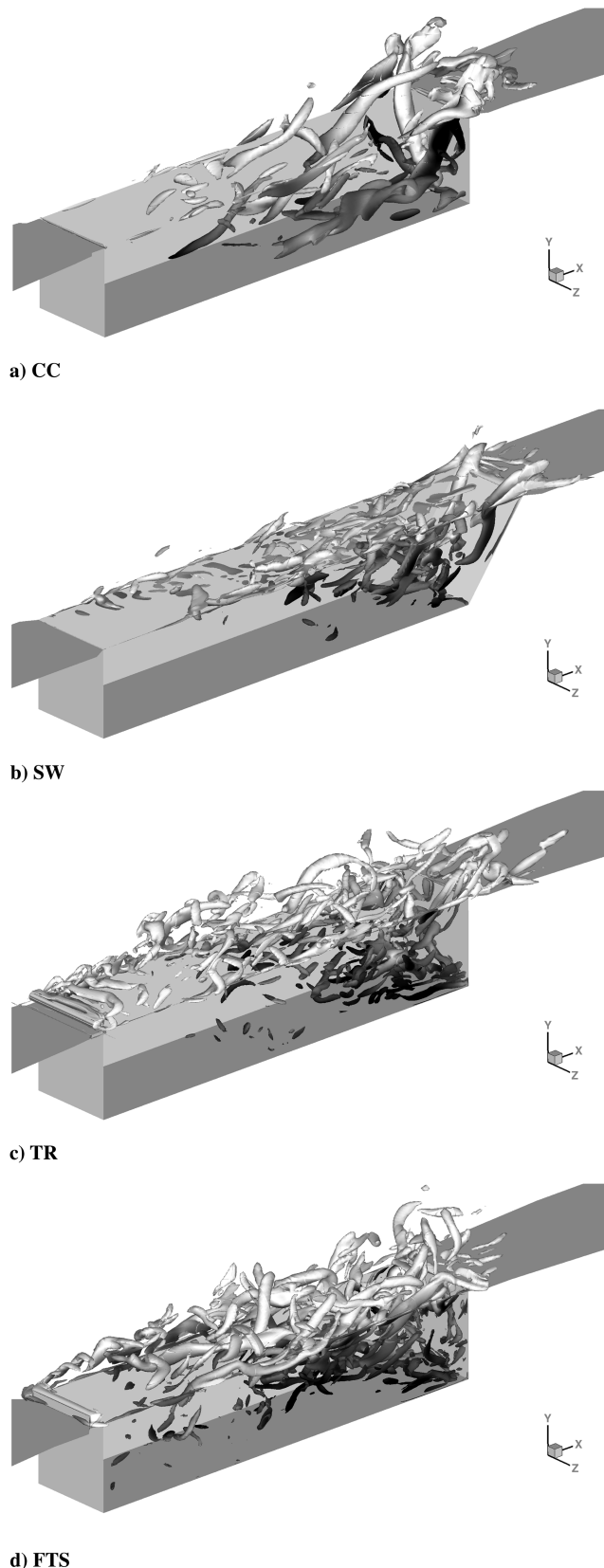


**Fig. 14** Instantaneous isosurfaces of  $Q$  criteria for the clean-cavity and passive flow control devices. Isosurfaces at  $Q = 2000$  are shown and colored with streamwise velocity and all plots at time,  $t = 0.06166$  s.

Figures 20a and 20b show samples of the time-varying forces on the fore and aft walls of the cavity for the four different configurations. This shows that the traces for both leading-edge devices still contained high-frequency oscillations, although the

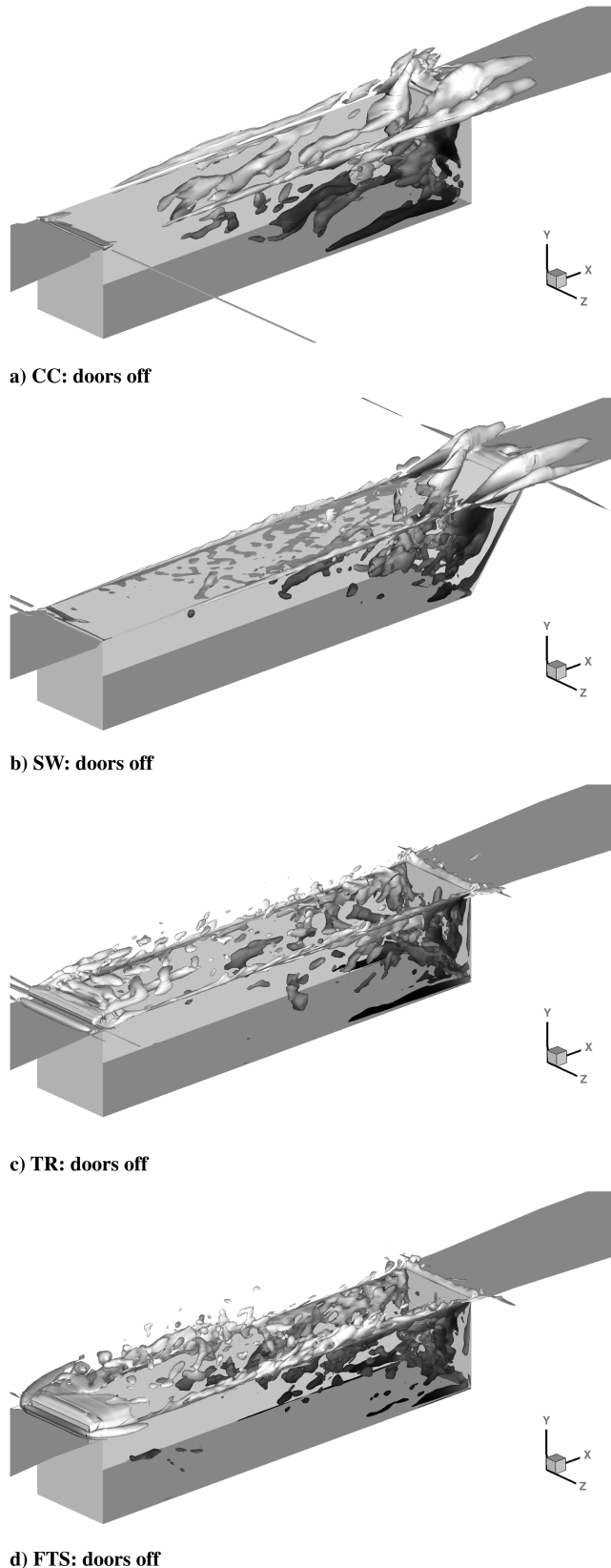


**Fig. 15** Time-averaged isosurfaces of  $Q$  criteria for the clean-cavity and passive flow control devices. Isosurfaces at  $Q = 150$  are shown and colored with streamwise velocity.

fluctuations were smaller in magnitude than for the clean cavity. However, the traces for the slanted aft wall did not contain the high-frequency oscillations shown by the other three cases, which was especially apparent at the front wall, where only a very low-frequency oscillation could be seen.

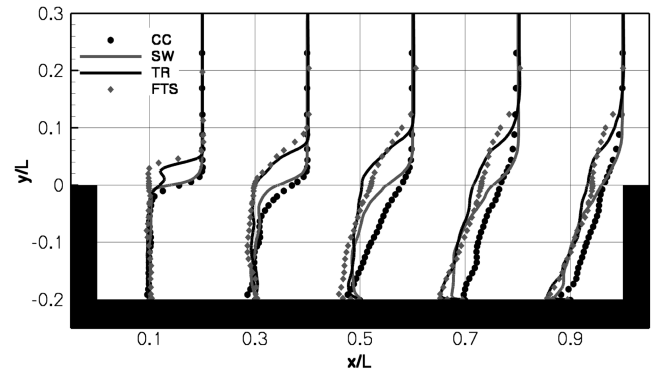


**Fig. 16** Averaged streamwise velocity profiles at the cavity centerline for the clean-cavity and the three flow control devices.

Figure 20c presents a summary for all cavity walls, with the vertical bars representing the average force coefficient and the error bars representing the minimum and maximum fluctuations in the instantaneous values. The averaged values show that the flat spoiler was the most effective device, because it reduced the forces on the four out of the five cavity walls. Only at the aft wall was the transverse rod more effective. As noticed in the traces, the main effect of the slanted aft wall was to reduce the force fluctuations on the walls.

Table 7 summarizes the reduction in averaged forces on the walls of the cavity for the three flow control configurations. It can be seen that the force on the aft wall was reduced by over 8% by slanting it at an angle to the oncoming flow. By adding a leading-edge flattop spoiler, the forces on the aft wall decreased by over 10%; however, the transverse rod had the largest reduction at over 12%.

## D. POD Modes

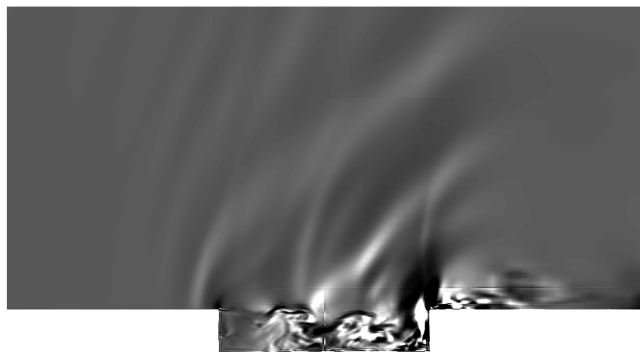
### 1. Pressure Traces

An initial investigation into the POD of the three-dimensional cavity was done using the signals from probes placed in the flow. For the clean-cavity case, 250 probes were specified in the cavity, forming a course grid over which the POD decomposition could be performed.

Figure 21 shows reconstructions of a pressure signal using 10, 50, and 154 modes, which equated to 65.9, 88.5, and 99.0% of the flow energy, respectively. Also shown in the figure are the frequency spectra, which give a clear picture of the effect of increasing the number of modes when trying to reconstruct the original signal. It can be seen that using 10 modes to reconstruct the data preserved the frequency spectrum with reasonable accuracy below a frequency of 1 kHz. Very little content was preserved above this value; however, it might be satisfactory to reconstruct the pressure signal accurately for the lower frequencies as long as the high-intensity tones are reconstructed well. From this result, it might be the case that storing as few as 10 modes might be sufficient.

When the number of modes used for the reconstruction was increased to 50, the pressure signal was captured with more accuracy. Looking at the time signal, the amplitudes of the peaks are better represented and more of the detail is captured. This was also reflected in the frequency spectra, in which the reconstructed data were very close to the original data for the lower-frequency peaks. Much more of the higher-frequency content was also preserved.

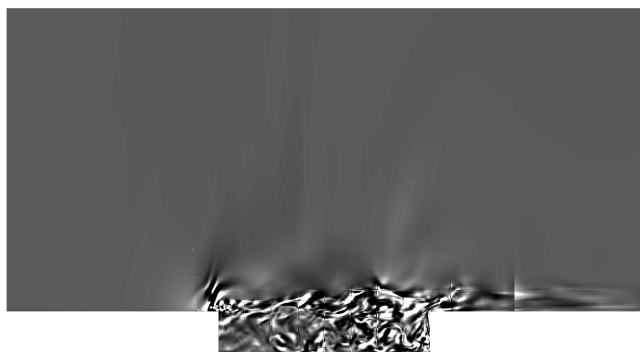
The reconstruction using 154 modes contained few discrepancies when compared with the original data. The pressure signals for both curves were almost identical and there was only a small difference for the high-frequency parts. In conclusion, it can be seen that the low-frequency part of the signal can be represented with relatively few modes. The peaks in the low-frequency end of the spectrum are caused by the large structures in the flow, and so these can be captured with a small amount of modes.



a) CC



b) SW



c) TR

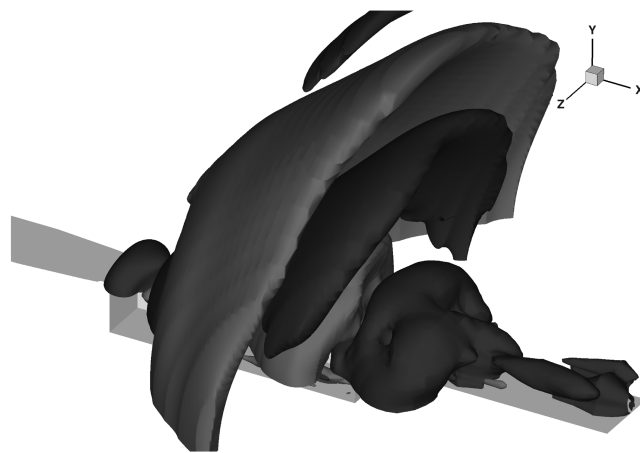


d) FTS

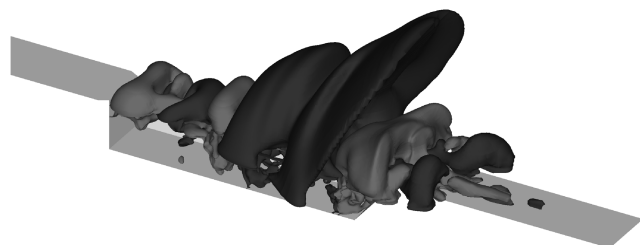
Fig. 17 Instantaneous dilatation at the cavity center plane for the clean-cavity and the passive flow control devices. All plots are at time  $t = 0.06166$  s.

## 2. Flowfield Data

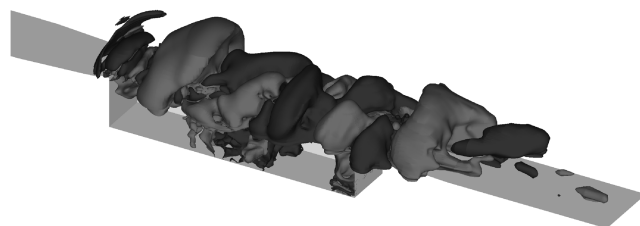
POD was then applied to the flowfield of the full three-dimensional clean cavity. To construct the POD modes, 50 snapshots were taken at regular intervals in the flow over a time period equal to one period of the first Rossiter mode. The pressure flowfield was then reconstructed using 10 or 20 modes. Figures 22a and 22b show the original flowfield at a time instant and a reconstruction using 10 modes. For clarity, slices down the center plane of the cavity are shown. It can be seen that although the two flowfields look similar, the reconstruction lacked some of the small-scale detail of the original. Figure 22d shows that areas close to the shear layer toward the rear of the cavity were most affected. However, even though only a small number of modes were used, the maximum difference



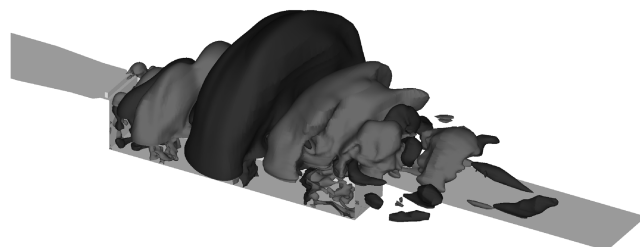
a) CC



b) SW

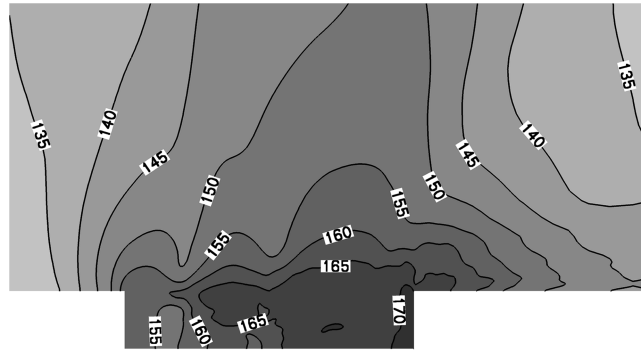


c) TR

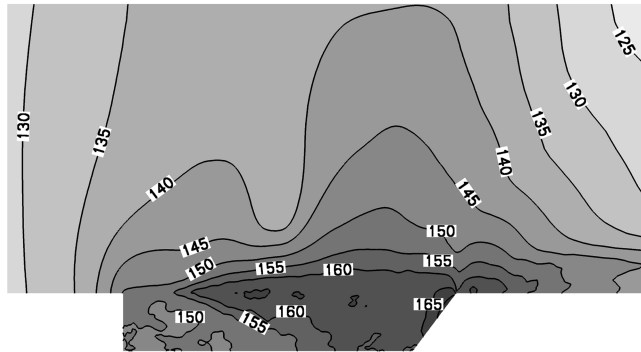


d) FTS

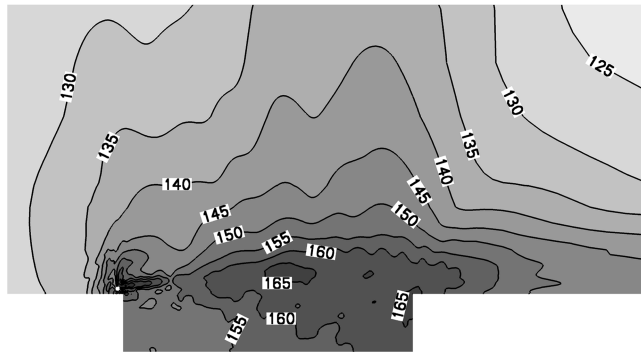
Fig. 18 Instantaneous isosurfaces of unsteady pressure for the clean-cavity and the passive flow control devices. Isosurface levels correspond to  $\pm 100$  dB and all plots at time,  $t = 0.06166$  s.



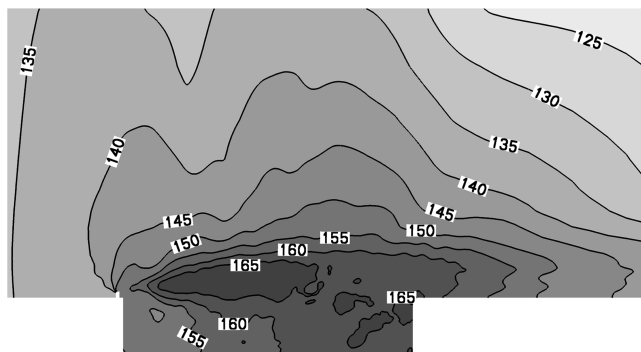
a) DES CC



b) DES SW



c) DES TR



d) DES FTS

**Fig. 19** OASPL contours at the cavity center plane for the clean-cavity and the three flow control devices.

between the original and the reconstruction was less than 5% anywhere in the flow.

When the number of modes was increased to 20 (Fig. 22c), the reconstruction improved, although it still lacked the small-scale detail of the original. Figure 22e shows that the difference between the two flowfields was much less than when using only 10 modes. However, the maximum difference was still approximately 5% at any point in the flow. This behavior was expected, due to the broad spectrum of flow scales and the fact that energy is still significant, even in higher frequencies of the spectrum.

### 3. Mode Shapes

Isosurfaces for the first two modes of pressure for the clean cavity, slanted aft wall and transverse rod are shown in Fig. 23. After studying the flowfield for each of the cases, some assumptions on what the structures represent could be drawn. The first mode for the clean cavity contained large structures around the aft wall and outside the cavity, which were not represented in the first mode for the other two cases. These structures could be associated with the acoustic waves propagating out of the cavity as a result of the shear-layer interaction with the aft wall. This also suggests that these acoustic waves contained a large portion of the energy within the flow because they existed in the first POD mode. Large structures were also located over the aft wall for the other two cases, although they were smaller in size. This was due to the smaller interaction of the shear layer with the aft wall. Also, structures existed in the front part of the cavity for the transverse rod case, whereas in the slanted-aft-wall case, the structures were confined to the rear of the cavity.

The structures in the second POD mode were much more confined to the cavity for all of the cases shown, although a large structure still existed over the aft wall for the clean cavity. The structures for the slanted aft wall were much smaller in size and still confined to the rear of the cavity. Structures of similar size and location existed in the second mode compared with the first for the transverse rod. The shedding from the rod could be seen in both modes, suggesting that the vortices contained large amounts of energy.

## E. Summary of Suppression Mechanisms

### 1. Cavities with Trailing-Edge Devices

The slanted aft wall reduced the OASPL across the cavity floor by the largest amount out of the three control devices. Visualizations of the results revealed the effects of the slanted aft wall, which are summarized as follows:

1) The first effect was shown to be the reduced level of acoustic generation at the aft wall. As the flow hits the surface at an angle, more was deflected out of the cavity rather than back into it.

2) The second effect was the reduced OASPLs inside the cavity. Visualizations of dilatation and the OASPL contours in Fig. 19 show that high levels of unsteadiness were confined to the area around the shear layer. This was due to the reduced levels of acoustic noise generation at the aft wall, and so the amount of acoustic propagation upstream in the cavity was reduced.

3) The third effect, shown from the analysis of the wall forces, was the stabilization of the shear layer. Plots of forces on the walls of the cavity showed that the averaged values were reduced little by slanting the aft wall. The largest reduction, about 8%, was gained over the aft wall. Analysis of the forces on the walls of the cavity showed that the main effect was not to reduce the absolute magnitude, but to reduce the frequency and magnitude of the oscillations caused by the unstable shear layer.

In clean-cavity flow the interaction of the shear layers with the aft wall creates a source of acoustic noise, which is then propagated upstream. These then interfere with the shear layer upstream and cause oscillations. The oscillations of the shear layer on the aft wall cause further acoustic radiation, and a feedback loop is generated. Therefore, because the initial acoustic radiation was significantly reduced in the slanted-aft-wall case, these results would suggest that the feedback loop that normally characterizes cavity flow was altered.

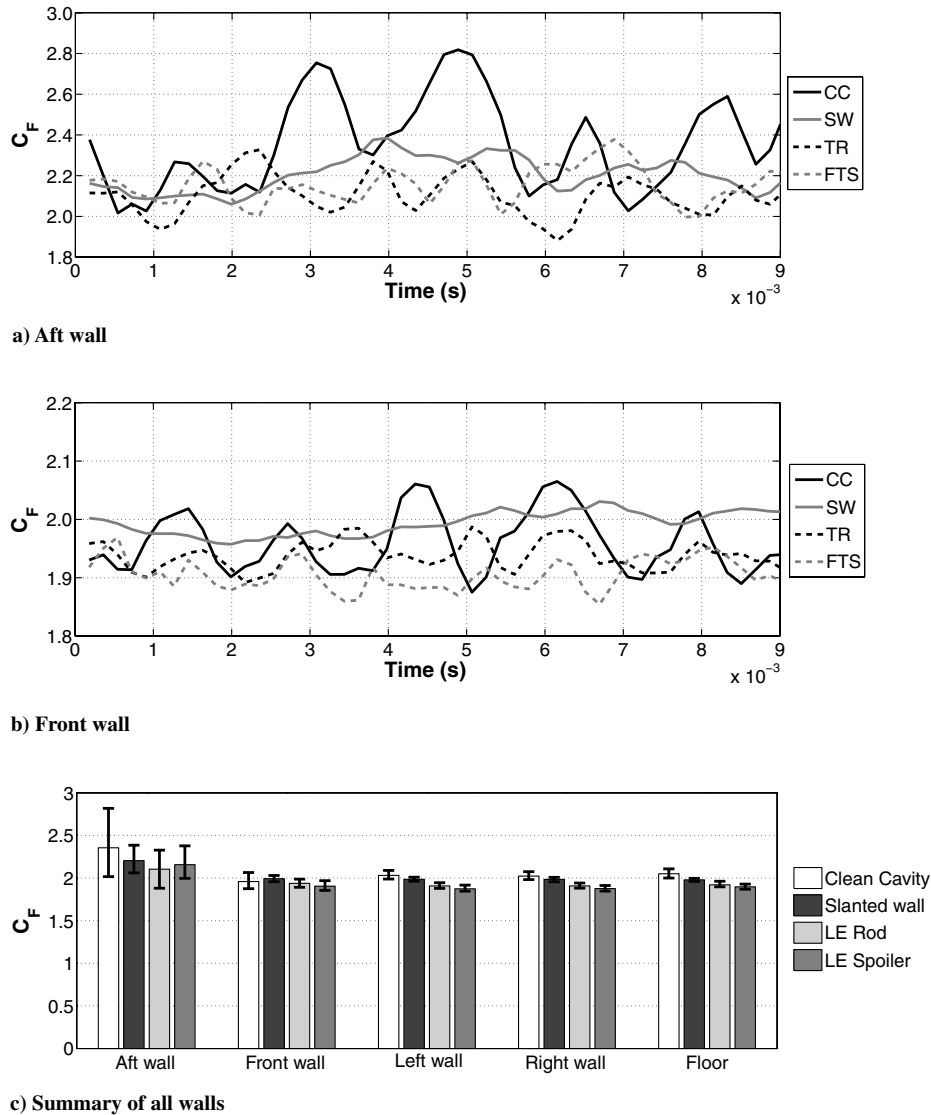


Fig. 20 Forces experienced by the walls of the cavity for the clean cavity and with passive flow control devices.

## 2. Cavities with Leading-Edge Devices

Both leading-edge control devices analyzed reduced the OASPL levels across the cavity floor by similar amounts, although the reduction was not as great as for the trailing-edge device, especially at the front of the cavity. Time-averaged flowfields showed that in both cases, the shear layer was lifted well above the aft wall. This meant that the mean forces experienced by the cavity walls were greatly reduced. The flattop lifted the shear layer higher than the transverse rod and so reduced the forces by the largest amount on all walls except the aft one. Instantaneous results showed that the shedding of the rod energized the shear layer, which remained stable for longer. This was also shown in the mean longitudinal velocity profiles, in which the profile for the flat spoiler in the aft part of the cavity was diffused much more than that of the transverse rod. Therefore, it was the transverse rod that actually minimized the interaction with the aft wall. However, the force traces for both devices still contained high-frequency oscillations on all walls, indicating that an unstable shear layer was still present, as in the clean-cavity case.

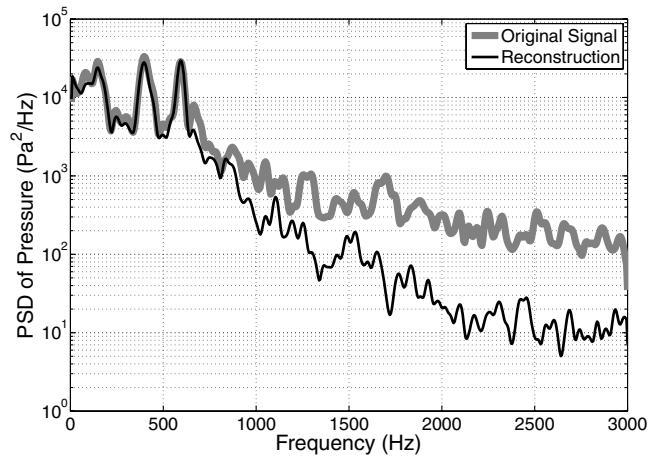
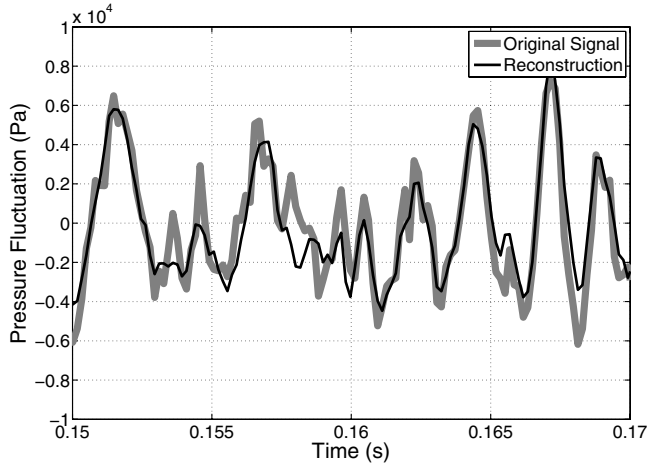
Dilatation visualizations revealed that high levels of unsteadiness still existed inside the cavity for both cases. However, for the two cases, this was due to two different reasons. For the flat spoiler, it was due to the earlier and more pronounced breakdown of the shear layer. In the case of the transverse rod, it was due to the rod forcing the shear layer at a higher frequency, and so extra content was added in the shear layer (as shown in the isosurfaces of  $Q$  criteria). Although this

initially had a positive effect in stabilizing the shear layer, it had a second effect in that higher-frequency oscillations were added, which caused more unsteadiness in the cavity. It was this that actually limited the reduction in noise levels inside the cavity for the transverse rod. Therefore, reducing the oscillations of the shear layer and thus minimizing the acoustic propagation inside the cavity, not just reducing the aft wall interaction, seems to be the key to reducing the OASPL on the floor. This was achieved by the slanted wall but not by the leading-edge devices.

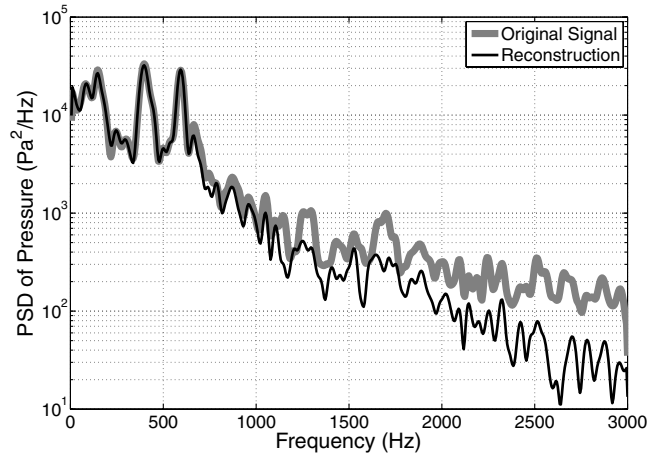
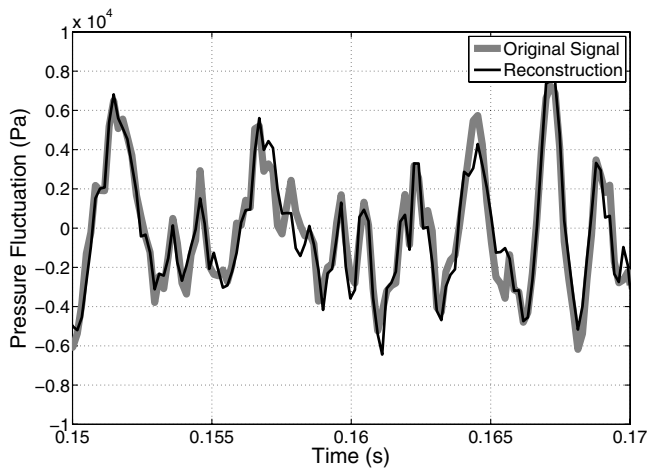
The leading-edge devices, did, however, reduce the OASPL outside the cavity to a larger extent than in the slanted-aft-wall case. The acoustic propagation seemed to depend solely on the interaction with the aft wall of the cavity, and because the transverse rod was the most successful at minimizing the interaction, it reduced the OASPL by the largest amount.

Table 7 Reduction in average forces on the cavity walls over the clean cavity for the three flow control devices using DES with the S-A turbulence model

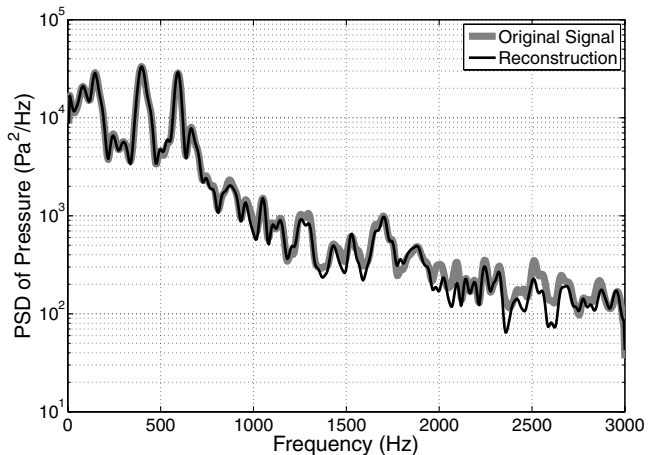
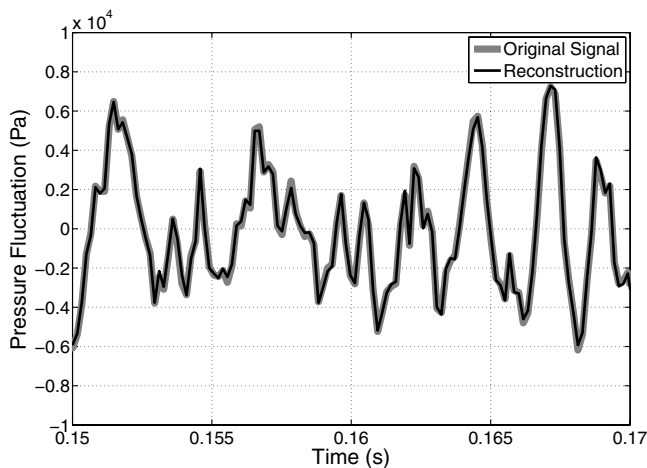
Location	SW	TR	FTS
Aft wall	6.37	10.63	8.41
Front wall	-1.75	1.05	2.72
Port wall	2.23	6.04	7.73
Starboard wall	1.91	5.70	7.42
Floor	3.50	6.34	7.50



a) Reconstruction of pressure signal using 10 modes (4% of total number of modes, 65.9% energy)



b) Reconstruction of pressure signal using 50 modes (20% of total number of modes, 88.5% energy)



c) Reconstruction of pressure signal using 154 modes (77% of total number of modes, 99.0% energy)

Fig. 21 Reconstructions of the pressure signal at the rear of the cavity (Kulite K29) for the clean-cavity configuration.

## VI. Conclusions

A systematic comparison has been presented between three passive open-loop devices for controlling the highly unsteady transonic cavity flow. The CFD predictions were based on the DES S-A model [50] and the results compared well against experimental data both in terms of the effectiveness of the devices and the

OASPL inside the cavity. Decomposition of the unsteady flow-fields into frequency bands suggested that DES was capable of resolving some of the most energetic bands of the spectrum and provided insight into the flow mechanism. The assessed leading-edge devices altered the feedback loop established in clean cavities via deflecting the shear layer above the cavity and via altering the flow near the cavity lip. They failed to remove any of the Rossiter

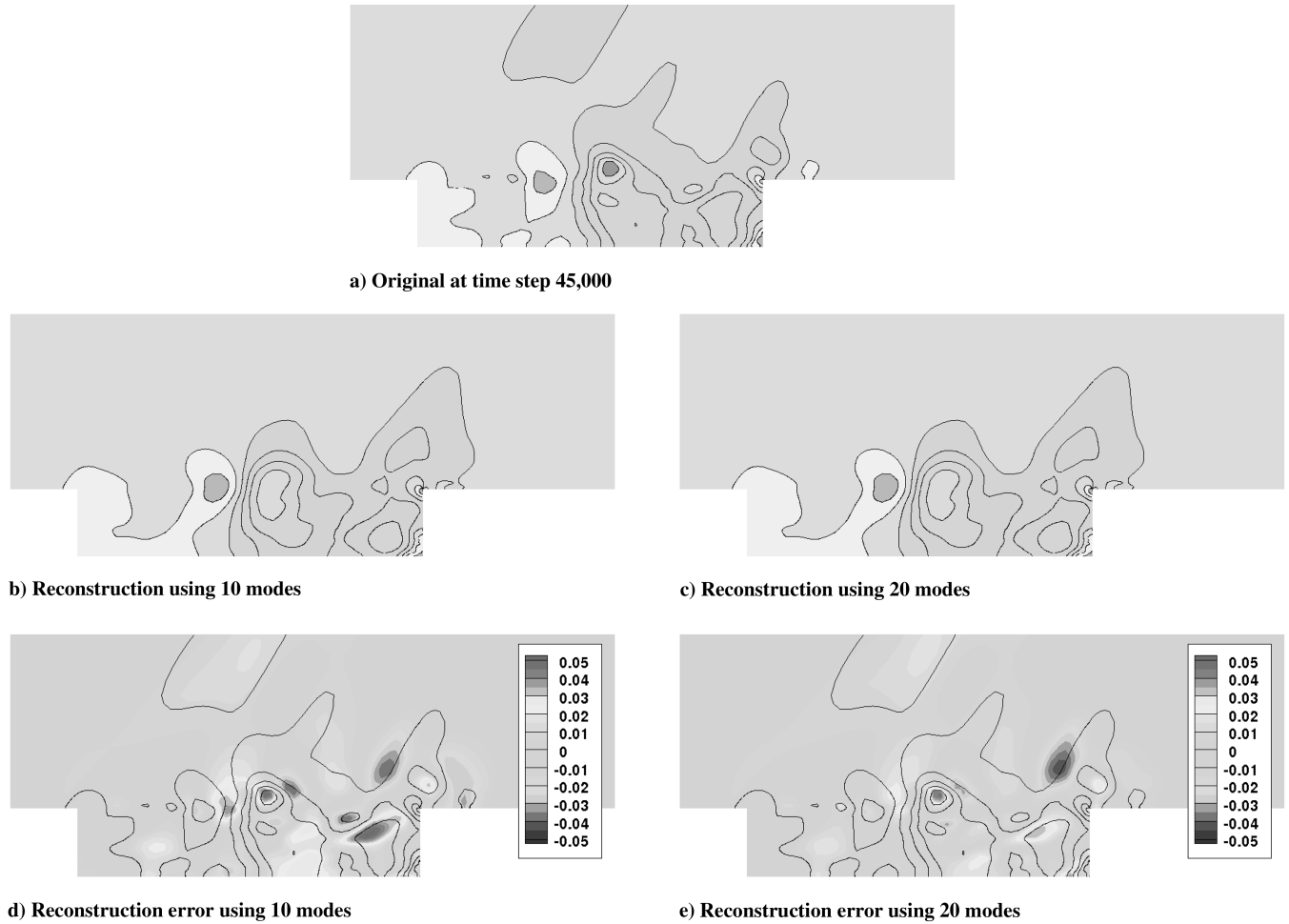


Fig. 22 Original flowfield compared with reconstruction using 10 and 20 modes for the clean-cavity configuration. Contours of pressure are shown.

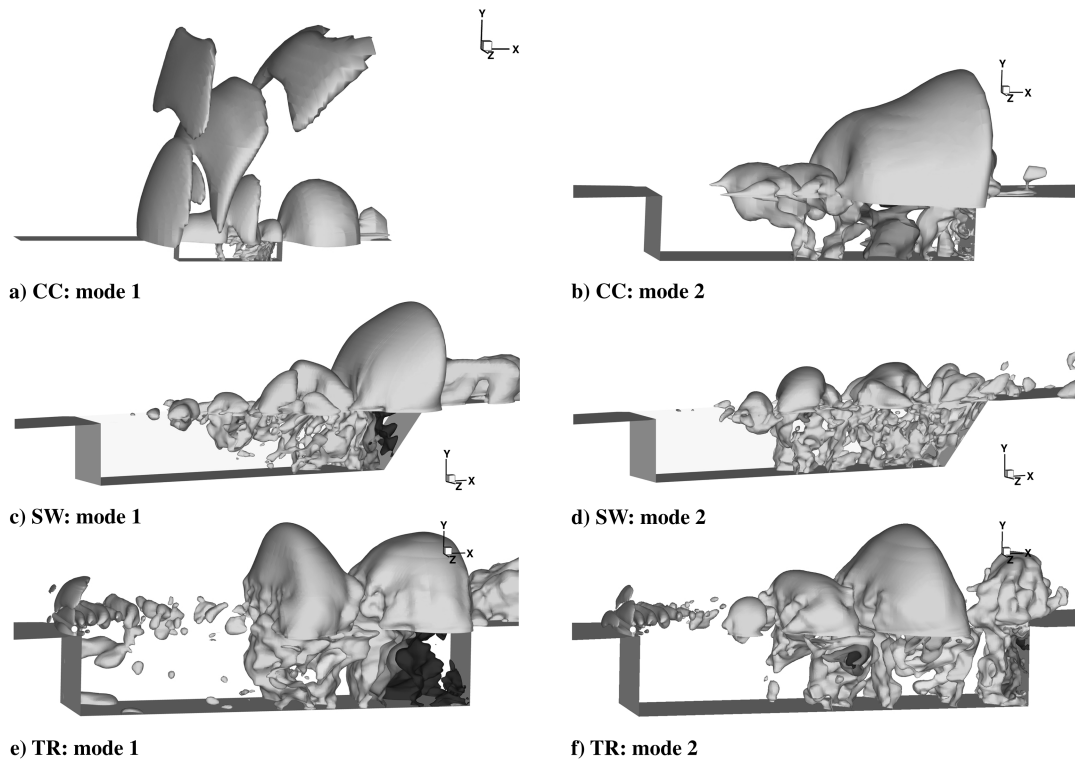


Fig. 23 First two POD modes of pressure for the clean cavity, slanted aft wall, and transverse rod. All isosurfaces are at the same values.

modes though. Instead, the modes were shifted to slightly higher frequencies and their energy was reduced. The trailing-edge device proved to be the most effective and worked by deflecting acoustic waves from the mouth of the cavity and keeping a more stable shear layer for longer along the cavity length. The visualized results revealed the preceding flow mechanisms with good accuracy and provided a wealth of information for this flow. The POD of the flow showed clear benefits in terms of data compression, though a significant number of modes were needed to reconstruct the details of the flowfield. Observations of the shape of the lower modes suggest that these are associated with the flow structures observed in the cavity. Overall, the CFD predictions were encouraging and put forward DES as a good tool for the study of cavity flows.

At present, efforts are directed toward the simulation of cavities with stores, aiming to reveal the relationship between the flow and forces that influence store release.

### Acknowledgments

The financial support of the Engineering and Physical Sciences Research Council through grant EP/C533380/1 is gratefully acknowledged. The authors would like to extend their gratitude to John Ross and Graham Foster of QinetiQ and Trevor Birch of Defense Science and Technology Laboratory (DSTL) for providing the experimental data.

### References

- [1] Rossiter, J., "A Preliminary Investigation into Armament Bay Buffet at Subsonic and Transonic Speeds," Royal Aircraft Establishment, TM AERO.679, Bedford, England, U.K., Aug. 1960.
- [2] Nayyar, P., "CFD Analysis of Transonic Turbulent Cavity Flows," Ph.D. Thesis, Univ. of Glasgow, Glasgow, Scotland, U.K., Aug. 2005.
- [3] Langtry, R., and Spalart, P., "Detached Eddy Simulation of a Nose Landing-Gear Cavity," *IUTAM Symposium Relation on Unsteady Separated Flows and Their Control* [CD-ROM], International Union of Theoretical and Applied Mechanics, June 2007.
- [4] Cattafesta, L., III, Song, Q., Williams, D., Rowley, C., and Alvi, F., "Active Control of Flow-Induced Cavity Oscillations," *Progress in Aerospace Sciences*, Vol. 44, Nos. 7–8, 2008, pp. 479–502; also AIAA Paper 2003-3567, 2003.  
doi:10.1016/j.paerosci.2008.07.002
- [5] Roshko, A., "Some Measurements of Flow in a Rectangular Cut-Out," NACA TP 3488, Aug. 1955.
- [6] Krishnamurty, K., "Acoustic Radiation from Two-Dimensional Rectangular Cutouts in Aerodynamic Surfaces," NACA TR 3487, Aug. 1955.
- [7] Rossiter, J., "Wind Tunnel Experiments on the Flow Over Rectangular Cavities at Subsonic and Transonic Speeds," Royal Aircraft Establishment, TR 64037, Bedford, England, U.K., Oct. 1964.
- [8] Tracy, M., Plentovich, E., and Chu, J., "Measurements of Fluctuating Pressure in a Rectangular Cavity in Transonic Flow at High Reynolds Numbers," NASA TM 4363, 1992.
- [9] Tracy, M., and Plentovich, E., "Characterization of Cavity Flow Fields Using Pressure Data Obtained in the Langley 0.3-Meter Transonic Cryogenic Tunnel," NASA TM 4436, Mar. 1993.
- [10] Tracy, M., and Plentovich, E., "Cavity Unsteady-Pressure Measurements at Subsonic and Transonic Speeds," NASA TP 3669, Dec. 1997.
- [11] Ross, J., and Peto, J., "Internal Stores Carriage Research at RAE," Royal Aircraft Establishment TR 2233, Bedford, England, U.K., Jan. 1992.
- [12] Ross, J., and Peto, J., "The Effect of Cavity Shaping, Front Spoilers and Ceiling Bleed on Loads Acting on Stores, and on the Unsteady Environment Within Weapon Bays," Royal Aircraft Establishment TR 2233, Bedford, England, U.K., Mar. 1997.
- [13] Ross, J., "Cavity Acoustic Measurements at High Speeds," QinetiQ, TR DERA/MSS/MSFC2/TR000173, Farnborough, England, U.K., Mar. 2000.
- [14] Nightingale, D., Ross, J., and Foster, G., "Cavity Unsteady Pressure Measurements—Examples from Wind-Tunnel Tests," Ver. 3, QinetiQ, Aerodynamics & Aeromechanics Systems Group, Farnborough, England, U.K., Nov. 2005.
- [15] Ritchie, S., Lawson, N., and Knowles, K., "An Experimental and Numerical Investigation of an Open Transonic Cavity," AIAA Paper 2003-4221, June 2003.
- [16] Shaw, L., Clark, R., and Talmadge, D., "F-111 Generic Weapons Bay Acoustic Environment," *Journal of Aircraft*, Vol. 25, No. 2, Feb. 1988, pp. 147–153.  
doi:10.2514/3.45555
- [17] Plentovich, E., Stallings, R., Jr., and Tracy, M., "Experimental Cavity Pressure Measurements at Subsonic and Transonic Speeds," NASA, TP 3358, 1993.
- [18] Stallings, R., Jr., Plentovich, E., Tracy, M., and Hemsch, M., "Effect of Passive Venting on Static Pressure Distributions in Cavities at Subsonic and Transonic Speeds," NASA TM 4549, June 1994.
- [19] Stallings, R., Jr., Plentovich, E., Tracy, M., and Hemsch, M., "Measurements of Store Forces and Moments and Cavity Pressures for a Generic Store in and Near a Box Cavity at Subsonic and Transonic Speeds," NASA TM 4611, May 1995.
- [20] Chung, K.-M., "Characteristics of Transonic Rectangular Cavity Flows," *Journal of Aircraft*, Vol. 37, No. 3, May 2000, pp. 463–468.  
doi:10.2514/2.2620
- [21] Chung, K.-M., "Three-Dimensional Effect on Transonic Rectangular Cavity Flows," *Experiments in Fluids*, Vol. 30, No. 5, 2001, pp. 531–536.  
doi:10.1007/s00348000232
- [22] Chung, K., "Characteristics of Compressible Rectangular Cavity Flows," *Journal of Aircraft*, Vol. 40, No. 1, Jan. 2003, pp. 137–142.  
doi:10.2514/2.3068
- [23] Kegerise, M., Spina, E., Garg, S., and Cattafesta, L., III, "Mode-Switching and Nonlinear Effects in Compressible Flow Over a Cavity," *Physics of Fluids*, Vol. 16, No. 3, Mar. 2004, pp. 678–686.  
doi:10.1063/1.1643736
- [24] Sarno, R., and Franke, M., "Suppression of Flow-Induced Pressure Oscillations in Cavities," *Journal of Aircraft*, Vol. 31, No. 1, Jan.–Feb. 1994, pp. 90–96.  
doi:10.2514/3.46459
- [25] Smith, B., Welterlen, T., Maines, B., Shaw, L., Stanek, M., and Grove, L., "Weapons Bay Acoustic Suppression from Rod Spoilers," 40th AIAA Aerospace Sciences Meeting and Exhibit, Reno, NV, AIAA Paper 2002-0662, Jan. 2002.
- [26] Ukeiley, L., Ponton, M., Seiner, J., and Jansen, B., "Suppression of Pressure Loads in Cavity Flows," *AIAA Journal*, Vol. 42, No. 1, Jan. 2004, pp. 70–79.  
doi:10.2514/1.9032
- [27] Baysal, O., Yen, G.-W., and Fouladi, K., "Navier–Stokes Computations of Cavity Aeroacoustics with Suppression Devices," *Journal of Vibration and Acoustics*, Vol. 116, Jan. 1994, pp. 105–112.  
doi:10.1115/1.2930385
- [28] Arunajatesan, S., Shipman, J., and Sinha, N., "Hybrid RANS-LES Simulation of Cavity Flow Fields with Control," 40th AIAA Aerospace Sciences Meeting and Exhibit, Reno, NV, AIAA Paper 2002-1130, Jan. 2002.
- [29] Comte, P., Daude, F., and Mary, I., "Simulation of the Reduction of the Unsteadiness in a Passively-Controlled Transonic Cavity Flow," *IUTAM Symposium Relation on Unsteady Separated Flows and Their Control* [CD-ROM], International Union of Theoretical and Applied Mechanics, June 2007.
- [30] Ashworth, R., "DES of a Cavity with Spoiler," *Notes on Numerical Fluid Mechanics-Advances in Hybrid RANS-LES Modelling*, Vol. 97, Springer, New York, 2008, pp. 162–171.
- [31] Baldwin, B., and Lomax, H., "Thin Layer Approximation and Algebraic Model for Separated Turbulent Flows," AIAA Paper 78-257, Jan. 1978.
- [32] Srinivasan, S., and Baysal, O., "Navier–Stokes Calculations of Transonic Flows Past Cavities," *Journal of Fluids Engineering*, Vol. 113, Sept. 1991, pp. 368–376.  
doi:10.1115/1.2909506
- [33] Tam, C.-J., Orkwis, P., and Disimile, P., "Algebraic Turbulence Model Simulations of Supersonic Open-Cavity Flow Physics," *AIAA Journal*, Vol. 34, No. 11, Nov. 1996, pp. 2255–2260.  
doi:10.2514/3.13388; also AIAA Paper 96-0075.
- [34] Rizzetta, D., "Numerical Simulation of Supersonic Flow Over a Three-Dimensional Cavity," *AIAA Journal*, Vol. 26, No. 7, July 1988, pp. 799–807.  
doi:10.2514/3.9972
- [35] Shih, S., Hamed, A., and Yeuan, J., "Unsteady Supersonic Cavity Flow Simulations Using Coupled  $k-\epsilon$  and Navier–Stokes Equations," *AIAA Journal*, Vol. 32, No. 10, Oct. 1994, pp. 2015–2021.  
doi:10.2514/3.12246
- [36] Zhang, X., "Compressible Cavity Flow Oscillation due to Shear Layer Instabilities and Pressure Feedback," *AIAA Journal*, Vol. 33, No. 8, Aug. 1995, pp. 1404–1411.  
doi:10.2514/3.12845
- [37] Rizzetta, D., and Visbal, M., "Large-Eddy Simulation of Supersonic

- Cavity Flowfields Including Flow Control," *AIAA Journal*, Vol. 41, No. 8, Aug. 2003, pp. 1452–1462.  
doi:10.2514/2.2128
- [38] Larchevêque, L., Sagaut, P., Mary, I., and Labbe, O., "Large-Eddy Simulation of a Compressible Flow Past a Deep Cavity," *Physics of Fluids*, Vol. 15, No. 1, Jan. 2003, pp. 193–210.  
doi:10.1063/1.1522379
- [39] Larchevêque, L., Sagaut, P., Lê, T.-H., and Comte, P., "Large-Eddy Simulation of a Compressible Flow in a Three-Dimensional Open Cavity at High Reynolds Number," *Journal of Fluid Mechanics*, Vol. 516, Oct. 2004, pp. 265–301.  
doi:10.1017/S0022112004000709
- [40] Larchevêque, L., Sagaut, P., and Labbe, O., "Large-Eddy Simulation of a Subsonic Cavity Flow including Asymmetric Three-Dimensional Effects," *Journal of Fluid Mechanics*, Vol. 577, Apr. 2007, pp. 105–126.  
doi:10.1017/S0022112006004502
- [41] Nayyar, P., Barakos, G. N., and Badcock, K. J., "Numerical Study of Transonic Cavity Flows Using Large-Eddy and Detached-Eddy Simulation," *The Aeronautical Journal*, Vol. 111, No. 1117, Mar. 2007, pp. 153–164.
- [42] Hamed, A., Basu, D., and Das, K., "Detached Eddy Simulations of Supersonic Flow Over Cavity," AIAA Paper 2003-0549, 2003.
- [43] Hamed, A., Basu, D., and Das, K., "Effect of Reynolds Number on the Unsteady Flow and Acoustic Fields of Supersonic Cavity," *4TH ASME/JSME Joint Fluids Engineering Conference*, Honolulu, HI, American Society of Mechanical Engineers Paper FEDSM2003-45473, New York, July 2003.
- [44] Mendonça, F., Allen, R., Charentenay, J., and Kirkham, D., "CFD Prediction of Narrowband and Broadband Cavity Acoustics at  $M = 0.85$ ," AIAA Paper 2003-3303, 2003.
- [45] Sinha, N., Arunajatesan, S., and Ukeiley, L., "High Fidelity Simulation of Weapon Bay Aeroacoustics and Active Flow Control," 6th AIAA/CEAS Aeroacoustics Conference, Lahaina, HI, AIAA Paper 2000-1968, June 2000.
- [46] Gloerfelt, X., Bogey, C., and Bailly, C., "Numerical Evidence of Mode Switching in the Flow-Induced Oscillations by a Cavity," *International Journal of Aeroacoustics*, Vol. 2, 2003, pp. 193–217.  
doi:10.1260/147547203322775533
- [47] Lai, H., and Luo, K., "A Three-Dimensional Hybrid LES-Acoustic Analogy Method for Predicting Open-Cavity Noise," *Flow, Turbulence and Combustion*, Vol. 79, No. 1, 2007, pp. 55–82.  
doi:10.1007/s10494-006-9066-y
- [48] Peng, S.-H., and Leicher, S., "DES and Hybrid RANS-LES Modelling of Unsteady Pressure Oscillations and Flow Features in a Rectangular Cavity," *Notes on Numerical Fluid Mechanics-Advances in Hybrid RANS-LES Modelling*, Vol. 97, Springer, New York, 2008, pp. 132–141.
- [49] Badcock, K., Richards, B., and Woodgate, M., "Elements of Computational Fluid Dynamics on Block Structured Grids Using Implicit Solvers," *Progress in Aerospace Sciences*, Vol. 36, No. 5–6, July 2000, pp. 351–392.  
doi:10.1016/S0376-0421(00)00005-1
- [50] Spalart, P., Jou, W.-H., Strelets, M., and Allmaras, S., "Comments on the Feasibility of LES for Wings, and on a Hybrid RANS/LES Approach," *First AFOSR International Conference on DNS/LES*, edited by C. Liu and Z. Liu, Advances in DNS/LES, Greyden Press, Columbus, OH, Aug. 1997, pp. 137–148.
- [51] Berkooz, G., Holmes, P., and Lumley, J., "The Proper Orthogonal Decomposition in the Analysis of Turbulent Flows," *Annual Review of Fluid Mechanics*, Vol. 25, 1993, pp. 539–575.  
doi:10.1146/annurev.fl.25.010193.002543
- [52] Chatterjee, A., "An Introduction to the Proper Orthogonal Decomposition," *Current Science*, Vol. 78, No. 7, April 2000, pp. 808–817.
- [53] Lumley, J., *Stochastic Tools in Turbulence*, Applied Mathematics and Mechanics, Vol. 12, Academic Press, New York, 1970.
- [54] Sirovich, L., "Turbulence and the Dynamics of Coherent Structures," *Quarterly of Applied Mathematics*, Vol. 45, No. 3, 1987, pp. 561–590.
- [55] Rowley, C., Colonius, T., and Murray, R., "Model Reduction for Compressible Flows Using POD and Galerkin Projection," *Physica D*, Vol. 189, Nos. 1–2, Feb. 2004, pp. 115–129.  
doi:10.1016/j.physd.2003.03.001
- [56] Podvin, B., Fraigneau, Y., Lusseyran, F., and Gougat, P., "A Reconstruction Method for the Flow Past an Open Cavity," *Journal of Fluids Engineering*, Vol. 128, No. 3, May 2006, pp. 531–540.  
doi:10.1115/1.2175159
- [57] Lawson, S., "Parallel Performance of Library Algorithms for Computational Engineering," M.S. Thesis, Univ. of Edinburgh, Edinburgh, England, U.K., Oct. 2007.
- [58] Childers, D. (ed.), *Modern Spectrum Analysis*, IEEE Press, New York, 1978, Chap. 2, pp. 23–148.
- [59] Pierce, A., *Acoustics: An Introduction to Its Physical Principles and Applications*, Acoustical Society of America, Woodbury, NY, 1989.
- [60] Ashworth, R., "Prediction of Acoustic Resonance Phenomena for Weapons Bays Using Detached Eddy Simulation," *The Aeronautical Journal*, Vol. 109, No. 1102, Dec. 2005, pp. 631–638.
- [61] Hunt, J., Wray, A., and Moin, P., "Eddies, Streams and Convergence Zones in Turbulent Flows," *Proceedings of the Summer Program*, N89-24555, Center for Turbulence Research, Stanford, CA, pp. 193–207, 1988.
- [62] Jeong, J., and Hussain, F., "On the Identification of a Vortex," *Journal of Fluid Mechanics*, Vol. 285, Feb. 1995, pp. 69–94.  
doi:10.1017/S0022112095000462